

AN1336: J/ψ production at forward rapidity in $p+p$ collision at
 $\sqrt{s} = 510$ GeV

M. Sarsour¹, T. Haseler¹, X. He¹, and R. Tieulent²

¹Georgia State University

²Universite de Lyon

November 27, 2019

Abstract

This analysis note details measurements of J/ψ meson reconstructed in the PHENIX muon arms as produced in $p+p$ collisions at $\sqrt{s} = 510$ GeV. The differential cross sections of J/ψ meson at $1.2 < |y| < 2.2$ versus p_T and rapidity are presented. The total cross section is, $Br(J/\psi \rightarrow \mu\mu) \times d\sigma/dy(1.2 < |y| < 2.2, 0 < p_T < 10 \text{ GeV}/c) = 54.3 \pm 0.5(\text{stat}) \pm 5.5(\text{syst})$ nb.

Contents

1	Introduction	4
2	Data set and Quality cuts	4
2.1	QA	4
2.2	Cuts	11
3	Data Analysis	14
3.1	Analysis code	14
3.2	Raw yield extraction	14
3.2.1	Background subtraction	14
3.2.2	Yield extraction	19
4	Acceptance and Reconstruction Efficiency	26
4.1	MuTr hit efficiency	41
5	Differential Cross Sections	43
6	Systematic Uncertainties	49
7	Results and Comparisons	50
7.1	Differential cross sections	50
7.2	$\langle p_T \rangle$ and $\langle p_T^2 \rangle$	54
7.3	$d\sigma/dy$ vs \sqrt{s}	56
A	Run Lists	59
B	PYTHIA Cards	60
C	Scaled down runs	61

Updates in this version

In this version of AN1336, the following parts of the analysis were updated:

- Adjusted the p_T and rapidity ranges as follows:
Rapidity distribution: from $0 < p_T < 9 \text{ GeV}/c \implies 0 < p_T < 10 \text{ GeV}/c$
 p_T distribution: from $0 < p_T < 15 \text{ GeV}/c \implies 0 < p_T < 10 \text{ GeV}/c$.
This was done to keep them consistent and the eliminated p_T bin $10 < p_T < 15 \text{ GeV}/c$ is very limited in statistics ($> 50\%$ statistical uncertainty) and covers very wide range ($5 \text{ GeV}/c$).
- Improved the input rapidity and p_T distributions so the simulation output matches that of the data
- Used GEANT4 instead of GEANT3.
- Carried out extensive study of the MuTr hit efficiency and its rate dependence
- Sampled all runs involved in the analysis to eliminate rate dependence and improve the embedding procedure

1 Introduction

J/ψ is a bound state of charm and anti-charm quark ($c\bar{c}$). Charmonium measurements in $p+p$ collisions are essential to the investigation of their production mechanisms. Combining this measurement with PHENIX measurements at 200 GeV [1] and LHC measurements at higher energies [2] allows testing theoretical approaches that are used to describe the hadronic production of charmonium. These models include the Color Evaporation Model (CEM) [3, 4], the Color Singlet Model (CSM) [5] and the Non-Relativistic Quantum Chromo-Dynamics model (NRQCD) [6]. Additionally, PHENIX published two J/ψ measurements [7, 8] at 510 GeV and it's important to have an associated cross section measurement.

This note presents an analysis calculating J/ψ differential cross sections as a function of rapidity and transverse momentum (p_T) in $p+p$ collisions at $\sqrt{s} = 510$ GeV. The data were collected in 2013 with the PHENIX muon arms.

2 Data set and Quality cuts

This analysis is of Run 13 $p+p$ data collected at $\sqrt{s_{NN}} = 510$ GeV that recorded by the PHENIX experiment. The data sample was produced using pro97 with 3.02×10^{12} MB events available on the Taxi. The taxi was run (TAXI #12079) using the macro and code that can be found in CVS:

```
offline/AnalysisTrain/pat/macro/Runpp2013lvm.C
```

```
offline/AnalysisTrain/picoDSTobject
```

which are used to produce picoDSTs as Run13pp510Muon dimuon output.

Dimuons are collected in the PHENIX muon arms using a dimuon trigger, ((**MUIDLL1_N2D||S2D**) ||(**N1D&&N2D**)&&**BBCLL1(noVtx)**). The picoDST code is used to reconstruct single muons as well as make dimuon pairs. This module is also used to make the mixed event pairs in which single muons paired together have a similar event vertex position within the detector system (in reference to the z -axis). The z -vertex used is within ± 30 cm of the origin, divided into bins with 2 cm widths and a pool depth of 10 is used to mix the events.

2.1 QA

The quality and assurance (QA) was done by the $W \rightarrow \mu$ analysis group and summarized in Ref. [9]. Runs were discarded based on the number of dead HV channels as well as hot/dead muon detector planes and packets. In the most recent analysis note from the $W \rightarrow \mu$ group, they identify run **397293** as representing "the average detector acceptance" well [10].

Given that the focus of the $W \rightarrow \mu$ group is on higher p_T region, a second run QA was done as a cross check to $W \rightarrow \mu$ group with a basic set of cuts were used (listed in Table 1) with the originally produced run list to look at dimuon event rates, north/south dimuon ratio and single muon kinematics. The distributions are shown below in Figures 1–9.

Considering the outcome of the second QA a new run list has been created in Appendix A. It removes runs in which a polarization measurement was made as well as any runs that are outliers from the means of several single and dimuon kinematic quantities. A total of 601 good runs survived the second QA and are used in the most recent analysis and are listed in Appendix A.

Table 1: Event, Track and DiMuon Selection Cuts used for the second QA

QA Cuts	North	South	
Event Cuts			
BBC _z	< 30	< 30	cm
Single Muon Selection Cuts			
DG0	< 14	< 22	cm
DDG0	< 10	< 10	degrees
χ_{Tr}^2	< 23	< 23	
N_{Tr} Hits	> 9	> 9	
N_{ID} Hits	> 5	> 5	
p_z	> 2.4	> 2.4	GeV/c
Lastgap	> 3	> 3	
Dimuon Selection Cuts			
$\chi_{EventVertex}^2$	< 5	< 5	
p_T	$0.0 < p_T < 7.0$	$0.0 < p_T < 7.0$	GeV/c

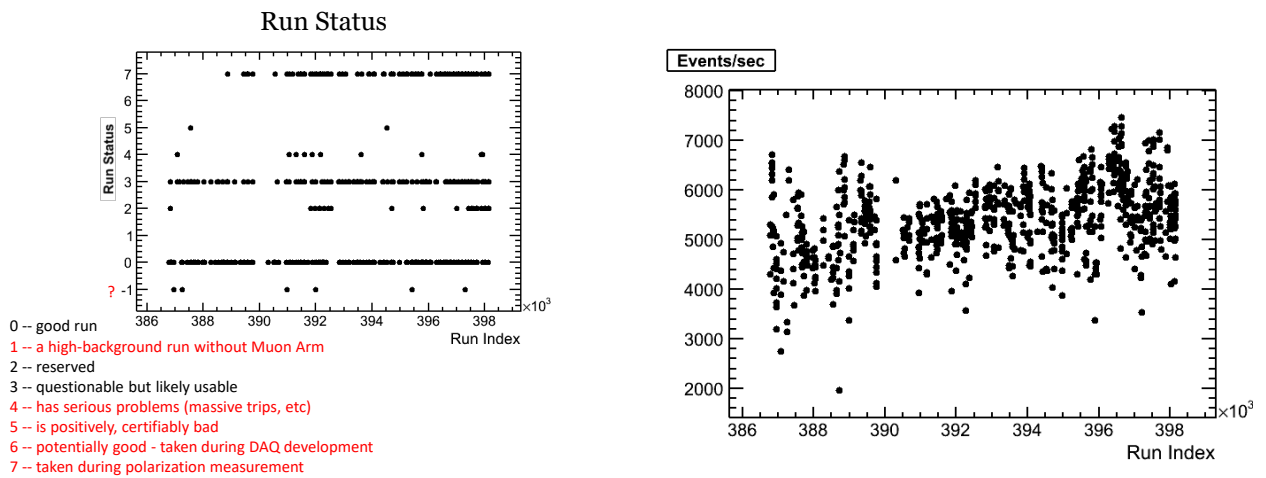


Figure 1: Left: DAQ status marked by shift leader. Right: Event rate for each run.

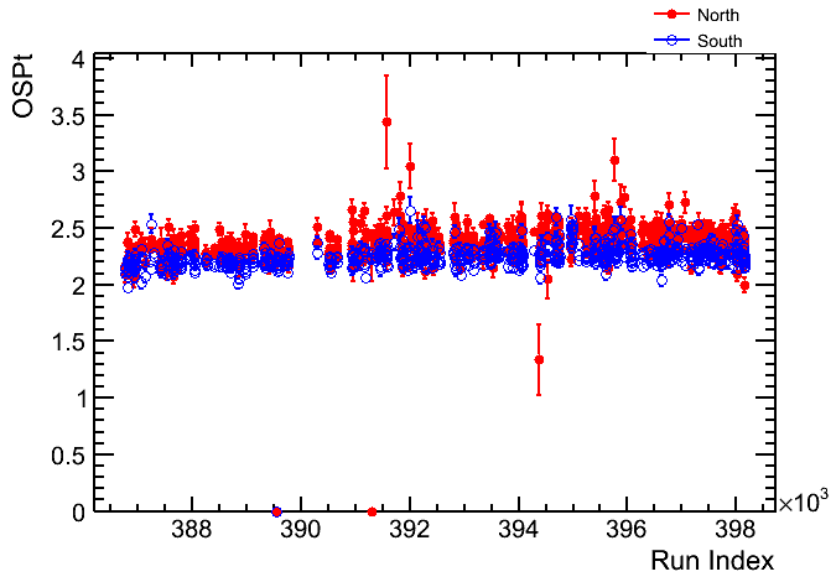


Figure 2: Dimuon mean p_T per run for the south arm (open blue circles) and for the north arm (closed red circles).

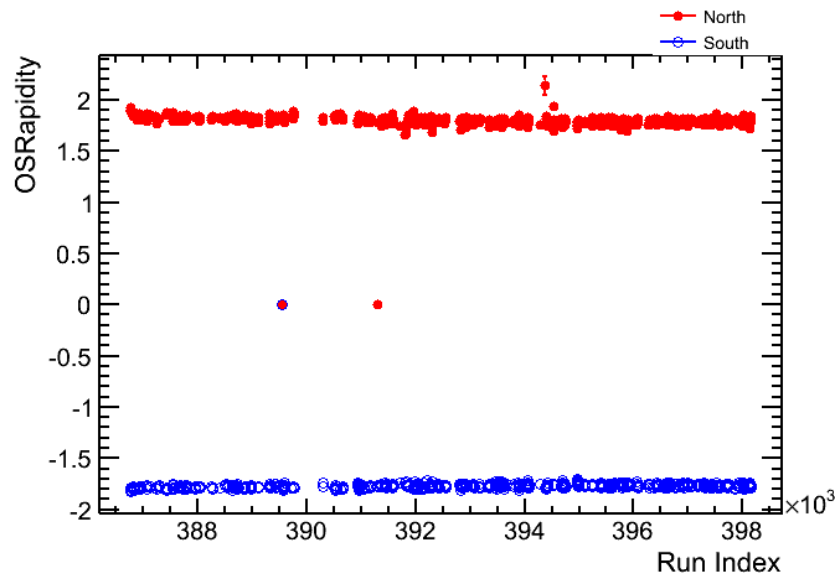


Figure 3: Dimuon mean y per run for the south arm (open blue circles) and for the north arm (closed red circles).

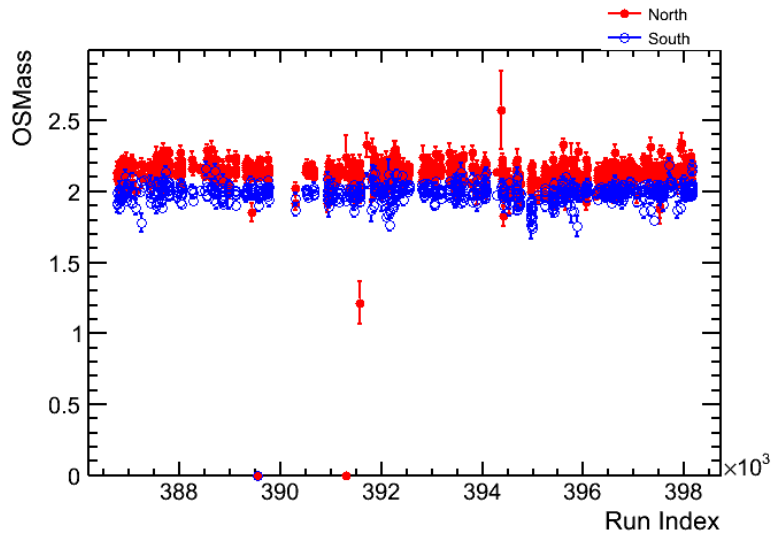


Figure 4: Dimuon mean mass per run for the south arm (open blue circles) and for the north arm (closed red circles).

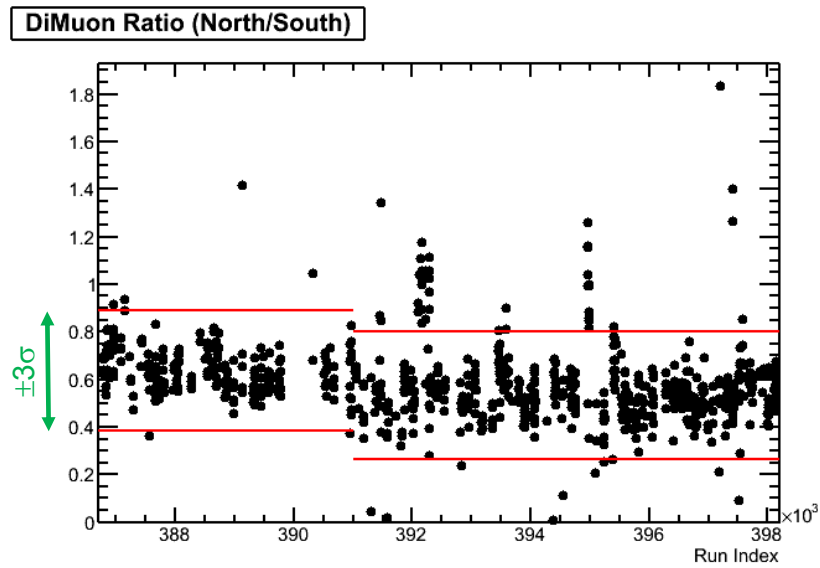


Figure 5: Dimuon ratio (North/South) per run.

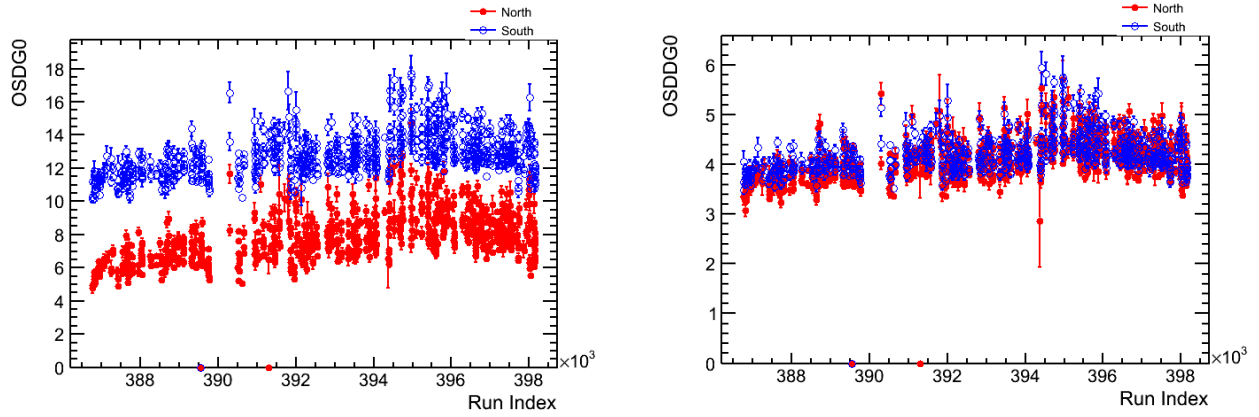


Figure 6: The mean of the single muon DG0 (left) and DDG0 (right) distributions for the north arm (closed red circles) and the south (open blue circles).

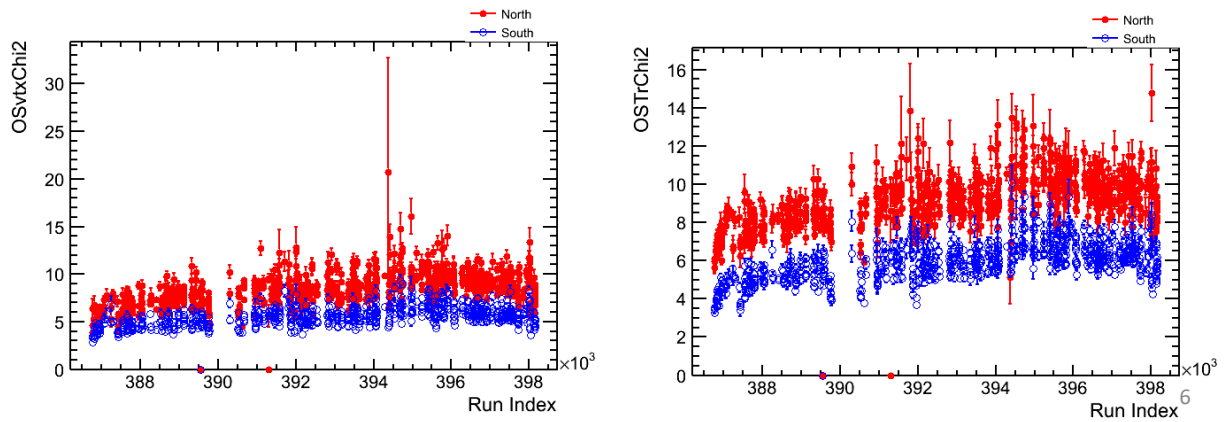


Figure 7: The mean of the single muon χ^2_{vtx} (left) and χ^2_{Tr} (right) distributions for the north arm (closed red circles) and the south (open blue circles).

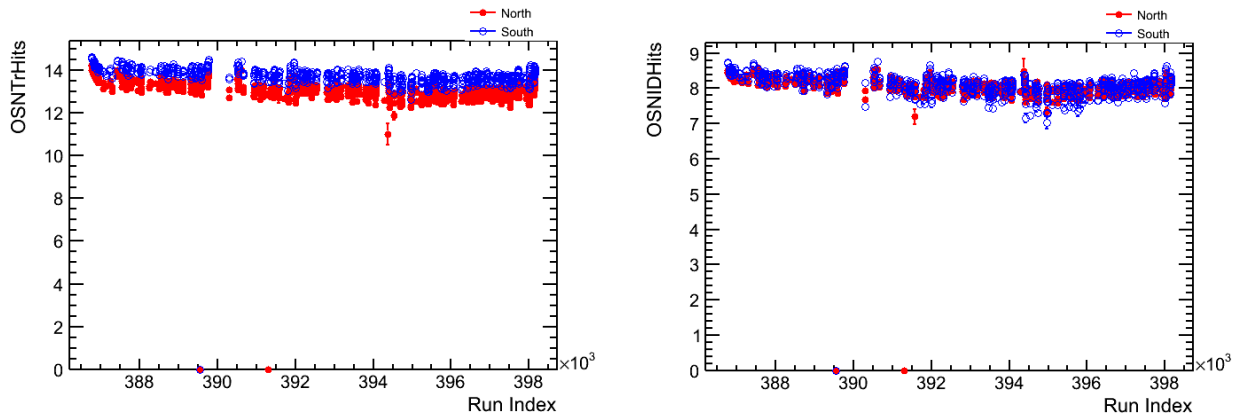


Figure 8: The mean of the single muon N_{TrHits} (left) and N_{IDHits} (right) distributions for the north arm (closed red circles) and the south (open blue circles).

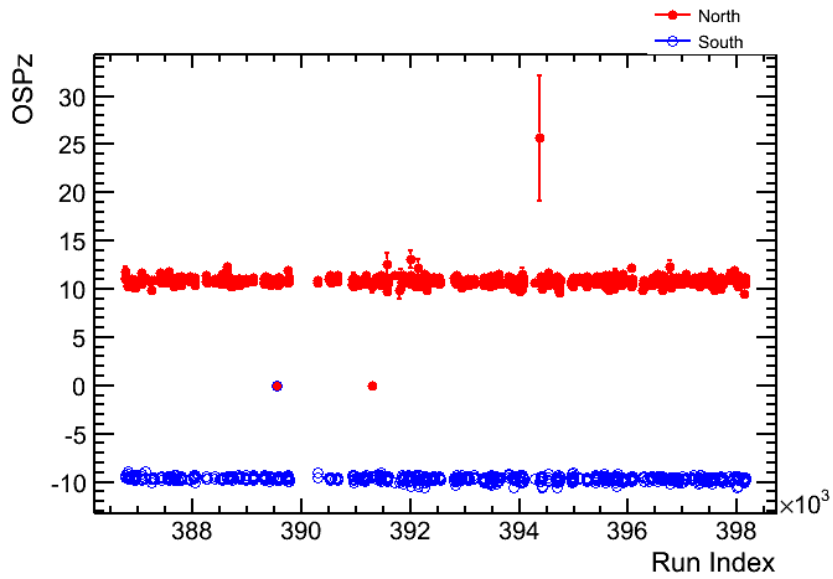


Figure 9: The mean of the single muon p_z distribution for the north arm (closed red circles) and the south (open blue circles).

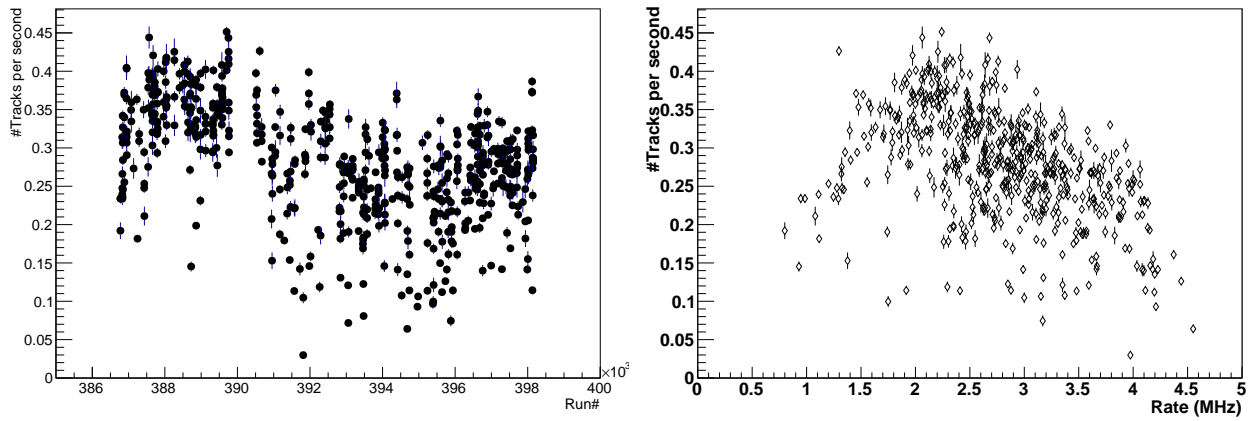


Figure 10: Left: Number of tracks used to produce the unlike-sign signal vs run number. Right: Number of tracks used to produce the unlike-sign signal vs live BBC rate.

2.2 Cuts

Cut levels have been adjusted in order to keep 99% of the J/ψ signal events with primary vertex around the nominal interaction point were selected such that $|BBC_z| < 30$ cm. Table 2 gives the selection cuts at the level of single muon as well as dimuon used in this analysis for both north and south arms. The value of each cut is chosen such that we keep as much of the signal as possible. However, since the distributions of the data and simulation are consistent the exact choice is not critical.

As a start for the analysis, the basic dimuon cuts, that were used in run-13 510 GeV ϕ meson analysis [11], are applied. However, this analysis is focused on J/ψ and the cuts were revisited in detail. The results of

Table 2: Track selection cuts used for north and south arms.

Variable	North Arm	South Arm
Single muon selections		
DG0	<15	<20
DDG0	<10	<10
Track χ^2	<23	<23
$ p_z $ (GeV/c)	>3.1	>3.0
# ID Hits	>6	>6
# Tr Hits	>9	>9
Lastgap	> 3	> 3
dimuon selections		
χ_{vtx}^2	<8	<6
y	$1.2 < y < 2.2$	
p_T (GeV/c)	$0 < p_T < 10$	

these studies are shown in Figures 11, 12, and 13 and led to the revised choices listed in Table 2.

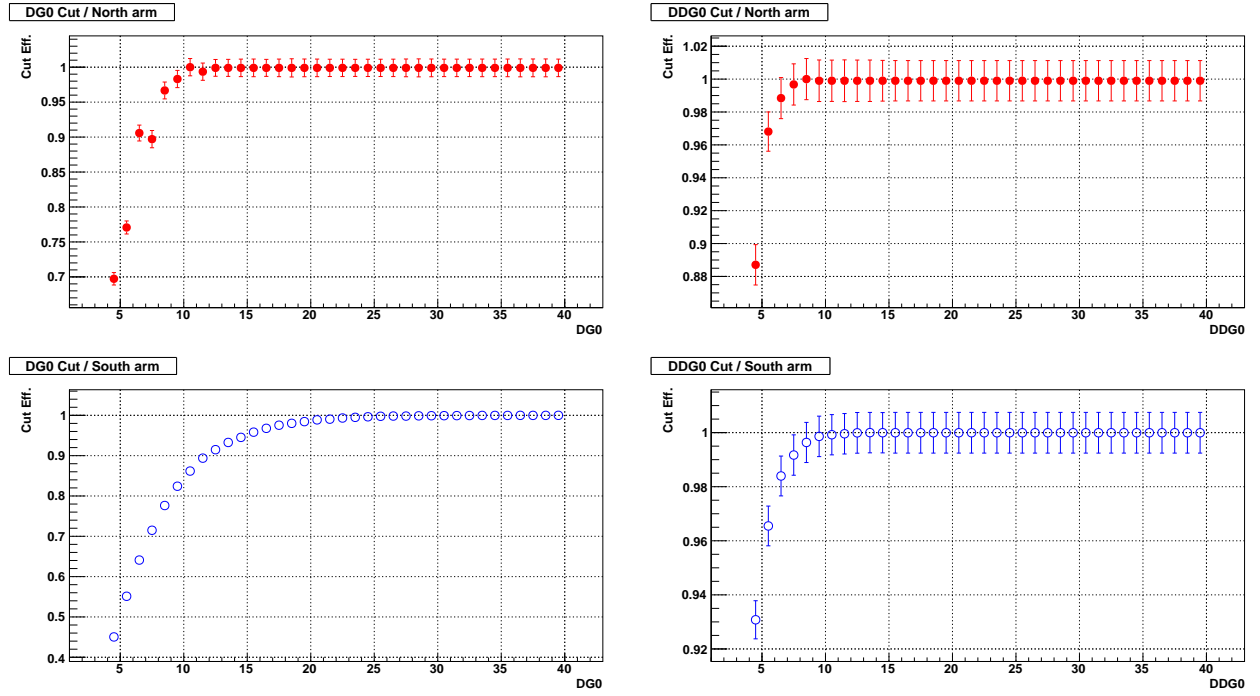


Figure 11: Left: the ratio of J/ψ signal with DG0 cut to J/ψ signal without DG0 cut for the north arm (top) and south arm (bottom). Right: the ratio of J/ψ signal with DDG0 cut to J/ψ signal without DDG0 cut for the north arm (top) and south arm (bottom).

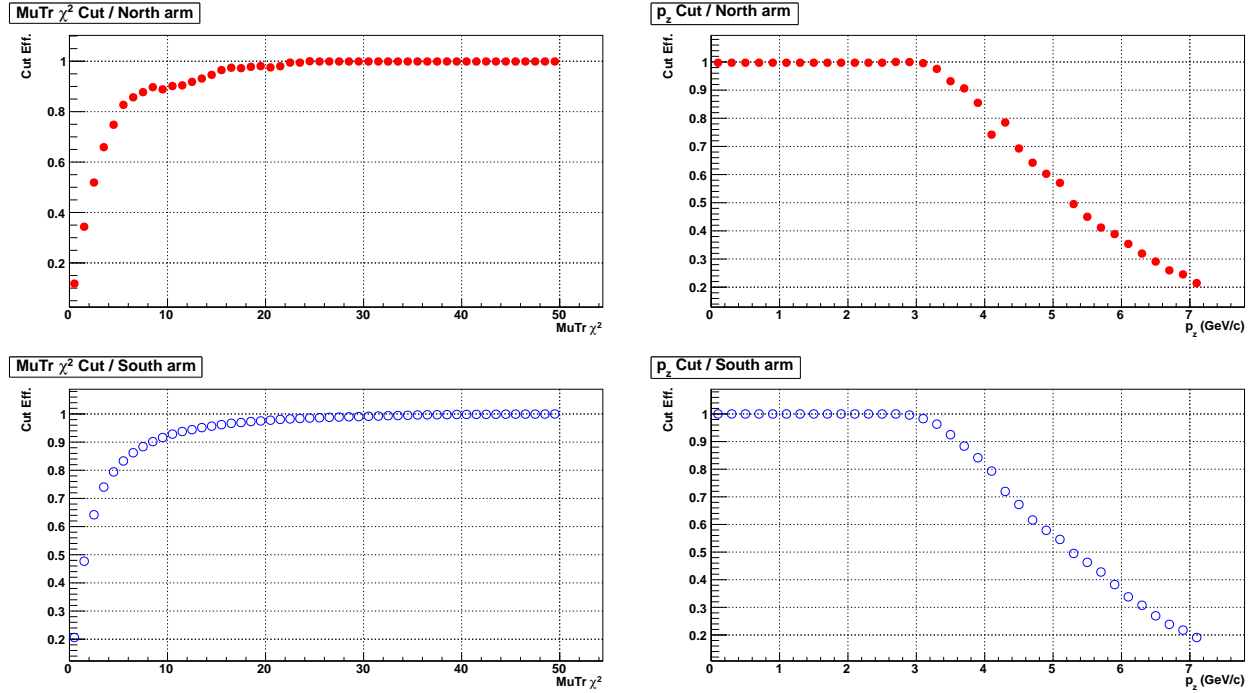


Figure 12: Left: the ratio of J/ψ signal with MuTr χ^2 cut to J/ψ signal without MuTr χ^2 cut for the north arm (top) and south arm (bottom). Right: the ratio of J/ψ signal with p_z cut to J/ψ signal without p_z cut for the north arm (top) and south arm (bottom).

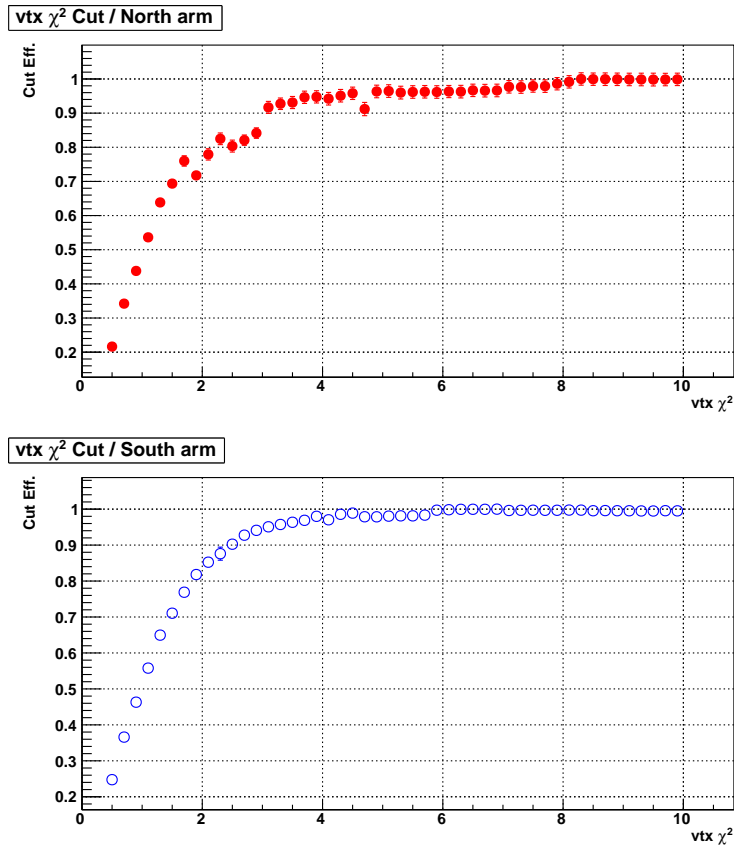


Figure 13: The ratio of J/ψ signal with χ_{vtx}^2 cut to J/ψ signal without χ_{vtx}^2 cut for the north arm (top) and south arm (bottom).

3 Data Analysis

3.1 Analysis code

The macro and code, used in this analysis, are in CVS:

```
offline/AnalysisTrain/pat/macro/Run_pp2013lvm.C
```

```
offline/AnalysisTrain/picoDST_object
```

```
offline/analysis/ppg222/sim_sar
```

which are used to produce picoDsts used in this analysis using TXAI#12079.

3.2 Raw yield extraction

3.2.1 Background subtraction

As discussed in Ref. [11], the uncorrelated combinatorial background is evaluated using two different techniques: like-sign pair spectrum and event mixing.

The combinatorial background extracted from the like-sign pair spectrum N_{CB}^{LS} is calculated according to:

$$N_{CB}^{LS} = 2R\sqrt{N_{++}N_{--}}, \quad \text{with} \quad R = \frac{N_{+-}^{mix}}{2\sqrt{N_{++}^{mix}N_{--}^{mix}}} \quad (1)$$

The R factor accounts for any difference in the acceptance between like-sign and unlike-sign pairs. Event mixing was performed by combining tracks from different events of similar vertex position, BBC_z , in the range $|BBC_z| < 30$ cm. The analysis of mixed event sample was performed using the same cut selections as the same event sample (see Table 2). The background spectrum calculated from event mixing N_{CB}^{mix} is the unlike-sign mixed pair distribution scaled such that its integral is the same as the combinatorial background spectrum calculated from the like-sign pair, as shown in Equation 1, in the invariant mass range 0.2 - 6.0 GeV/c²:

$$N_{CB}^{mix} = N_{+-}^{mix} \frac{\int N_{CB}^{LS} dM}{\int N_{+-}^{mix} dM} \quad (2)$$

Figures 14 and 15 show the like-sign and mixed events backgrounds after being normalized along with the unlike-sign signal sorted in different p_T bins over the range $0 < p_T < 10$ GeV/c, while Figures 16 and 17 show the like-sign and mixed events backgrounds along with the unlike-sign signal sorted in different rapidity bins and integrated over the range $0 < p_T < 10$ GeV/c.

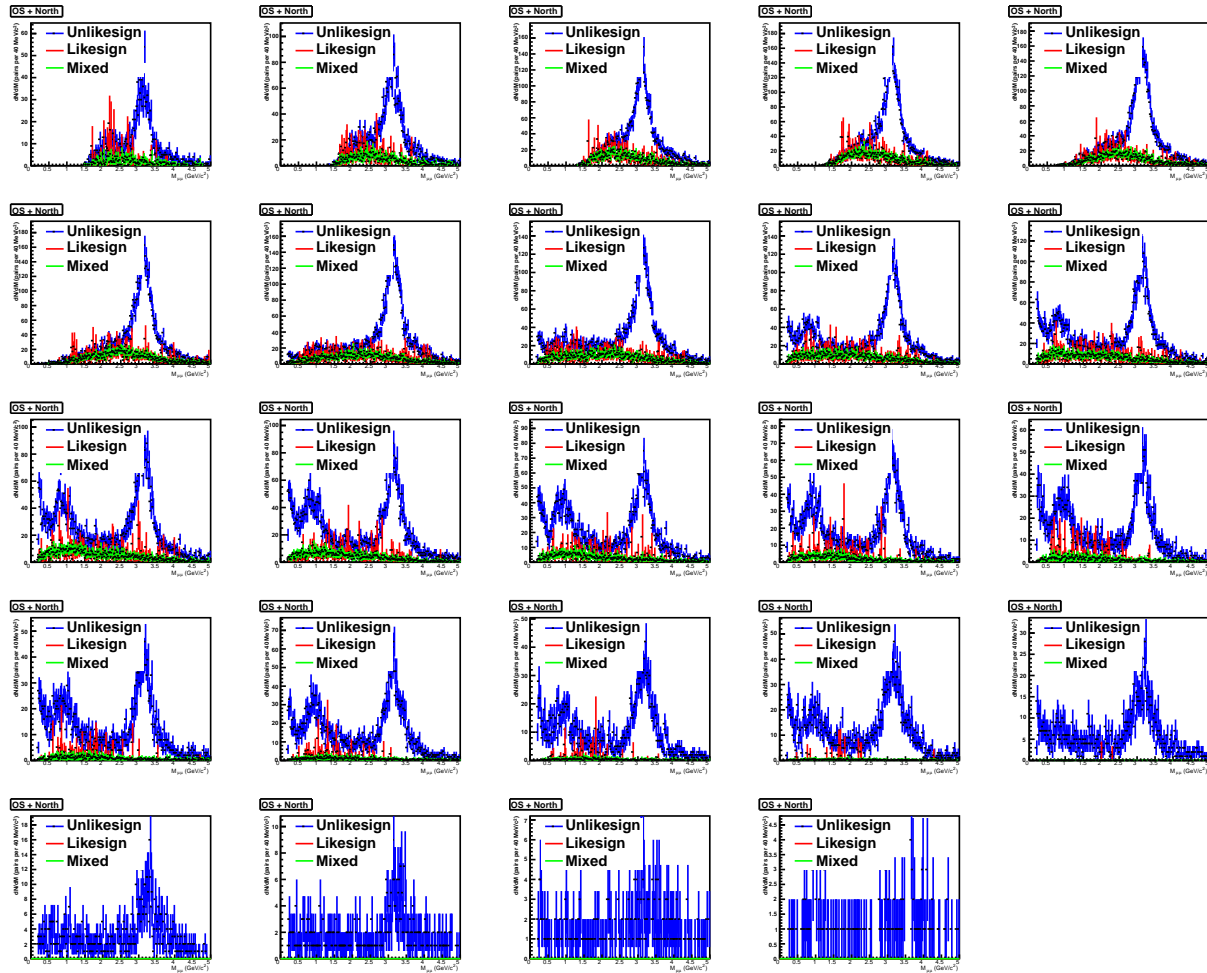


Figure 14: Unlike-sign mass spectra (blue points) and background spectra estimated using the like-sign pairs (red) and the event-mixing technique (green) for the north arm sorted in p_T .

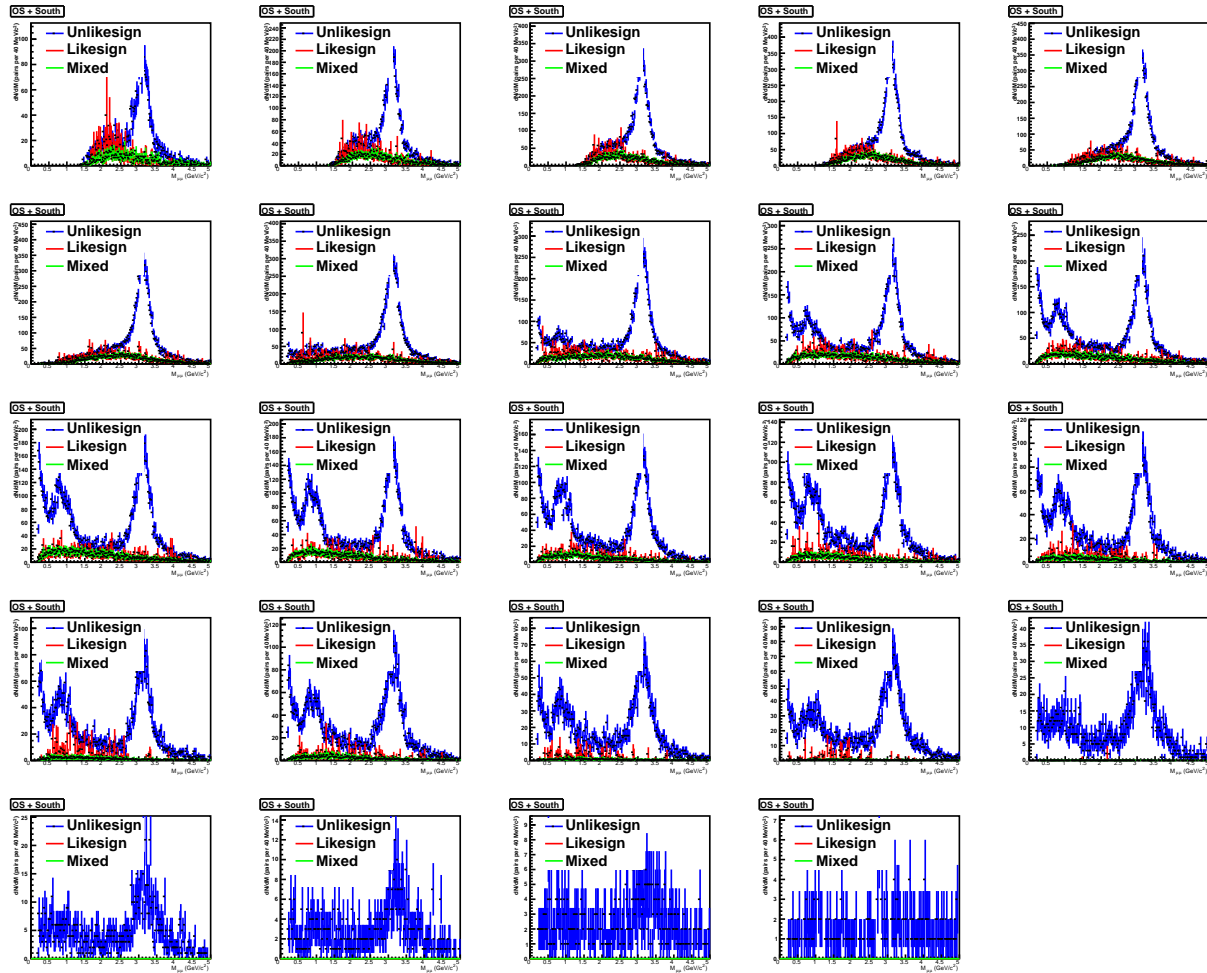


Figure 15: Unlike-sign mass spectra (blue points) and background spectra estimated using the like-sign pairs (red) and the event-mixing technique (green) for the south arm sorted in p_T .

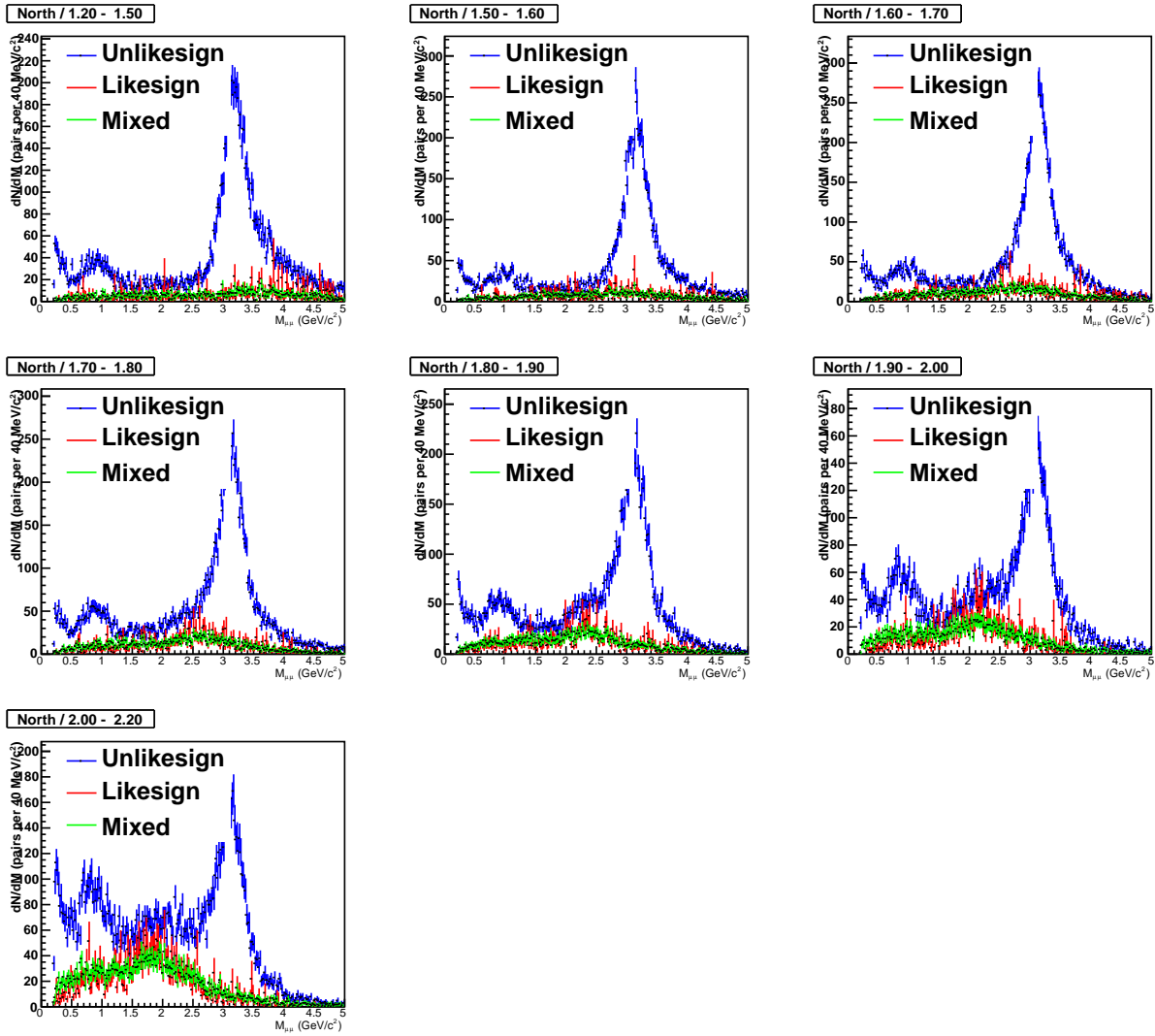


Figure 16: Unlike-sign mass spectra (blue points) and background spectra estimated using the like-sign pairs (red) and the event-mixing technique (green) for the north arm sorted in rapidity.

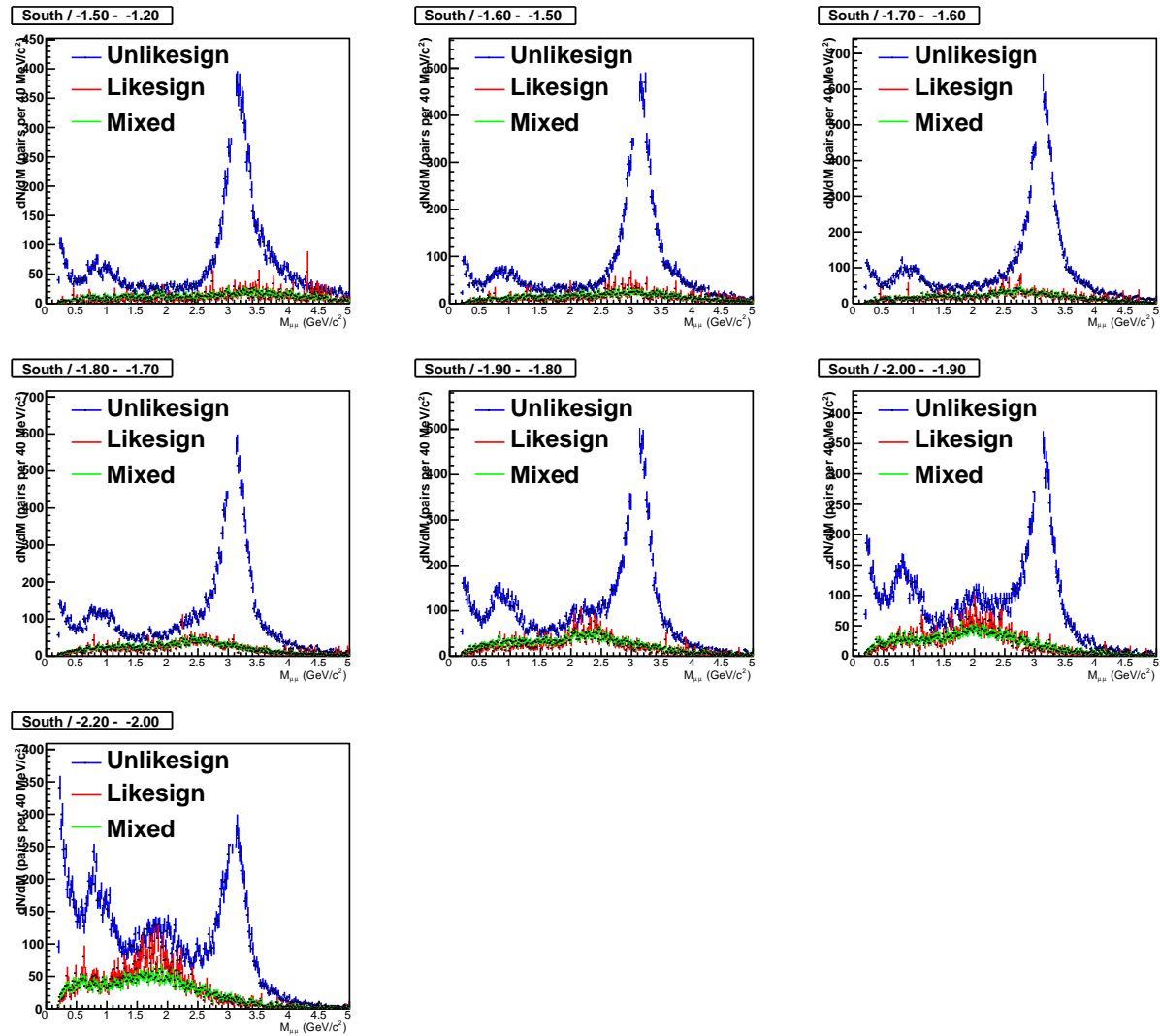


Figure 17: Unlike-sign mass spectra (blue points) and background spectra estimated using the like-sign pairs (red) and the event-mixing technique (green) for the south arm sorted in rapidity.

3.2.2 Yield extraction

The signal invariant mass spectrum is calculated by subtracting the uncorrelated combinatorial background spectrum from the unlike-sign spectrum. Both estimates of the uncorrelated combinatorial background agree, however, the like-sign method has much higher fluctuations and the mixed events method is used for uncorrelated background subtraction. The remaining correlated background is composed of open charm, open bottom and DY. After subtracting the uncorrelated background, the unlike-sign spectrum including the correlated background is fitted by the following function,

$$f(m_{\mu\mu}) = p_0 \left[\frac{(1-p_3)}{\sqrt{2\pi}p_2} \exp\left(-\frac{1}{2} \frac{(m_{\mu\mu} - p_1)^2}{p_2^2}\right) + \frac{p_3}{\sqrt{2\pi}p_4} \exp\left(-\frac{1}{2} \frac{(m_{\mu\mu} - p_1)^2}{p_4^2}\right) \right] + p_6 \exp(p_7 + p_8 m_{\mu\mu}) \quad (3)$$

This fit function is chosen based on previous PHENIX muon arm analyses [12]. The J/ψ shape is better described with two Gaussian distributions, corresponding to the first two terms in Equation 3, one for the J/ψ peak and a second one with larger width to account for the wide sides, which occurs due to limitations in MuTr resolution. An exponential is used to account for the continuum contributions from open charm, open bottom and DY which is the third term in Equation 3.

Figures 18 and 19 show the unlike-sign spectra after subtracting the mixed-events background for different p_T bins over the range $0 < p_T < 10$ GeV/c, while Figures 20 show the unlike-sign spectra after subtracting the mixed-events background for the different rapidity bins and integrated over the range $0 < p_T < 10$ GeV/c.

Figures 21 and 22 show the means and widths in the left and right panels, respectively, from these fits.

Figure 23 shows J/ψ yields (uncorrected for acceptance) as a function of p_T and rapidity, respectively, from these fits. Tables 3 and 4 lists J/ψ yields as a function of p_T and rapidity, respectively.

Table 3: J/ψ meson yield as a function of p_T for both south and north arms.

p_T (GeV/c)	$N_{J/\psi}$ ($1.2 < y < 2.2$)	$N_{J/\psi}$ ($-2.2 < y < -1.2$)
0.00 - 0.25	8.4e+02 ± 4.3e+01	1.9e+03 ± 8.1e+01
0.25 - 0.50	2.5e+03 ± 7.3e+01	5.8e+03 ± 1.0e+02
0.50 - 0.75	3.8e+03 ± 8.7e+01	8.0e+03 ± 1.3e+02
0.75 - 1.00	4.5e+03 ± 9.4e+01	9.6e+03 ± 1.3e+02
1.00 - 1.25	4.9e+03 ± 9.6e+01	1.0e+04 ± 1.3e+02
1.25 - 1.50	4.6e+03 ± 9.3e+01	9.5e+03 ± 1.3e+02
1.50 - 1.75	4.5e+03 ± 9.1e+01	8.8e+03 ± 1.3e+02
1.75 - 2.00	3.9e+03 ± 8.1e+01	7.4e+03 ± 1.2e+02
2.00 - 2.25	3.4e+03 ± 7.9e+01	6.6e+03 ± 1.1e+02
2.25 - 2.50	2.9e+03 ± 7.8e+01	5.6e+03 ± 1.3e+02
2.50 - 2.75	2.5e+03 ± 7.4e+01	5.1e+03 ± 9.6e+01
2.75 - 3.00	2.2e+03 ± 6.7e+01	4.4e+03 ± 8.9e+01
3.00 - 3.25	1.9e+03 ± 6.0e+01	3.8e+03 ± 9.6e+01
3.25 - 3.50	1.7e+03 ± 5.6e+01	3.1e+03 ± 7.9e+01
3.50 - 3.75	1.3e+03 ± 5.1e+01	2.6e+03 ± 6.9e+01
3.75 - 4.00	1.1e+03 ± 4.7e+01	2.1e+03 ± 6.5e+01
4.00 - 4.50	1.7e+03 ± 5.9e+01	3.2e+03 ± 7.8e+01
4.50 - 5.00	1.2e+03 ± 5.0e+01	2.2e+03 ± 6.4e+01
5.00 - 6.00	1.5e+03 ± 5.4e+01	2.6e+03 ± 7.2e+01
6.00 - 7.00	6.7e+02 ± 4.2e+01	1.2e+03 ± 5.0e+01
7.00 - 8.00	2.3e+02 ± 2.8e+01	5.0e+02 ± 3.5e+01
8.00 - 10.00	1.9e+02 ± 2.6e+01	3.4e+02 ± 3.2e+01
Total	5.2e+04 ± 3.2e+02	1.0e+05 ± 4.6e+02

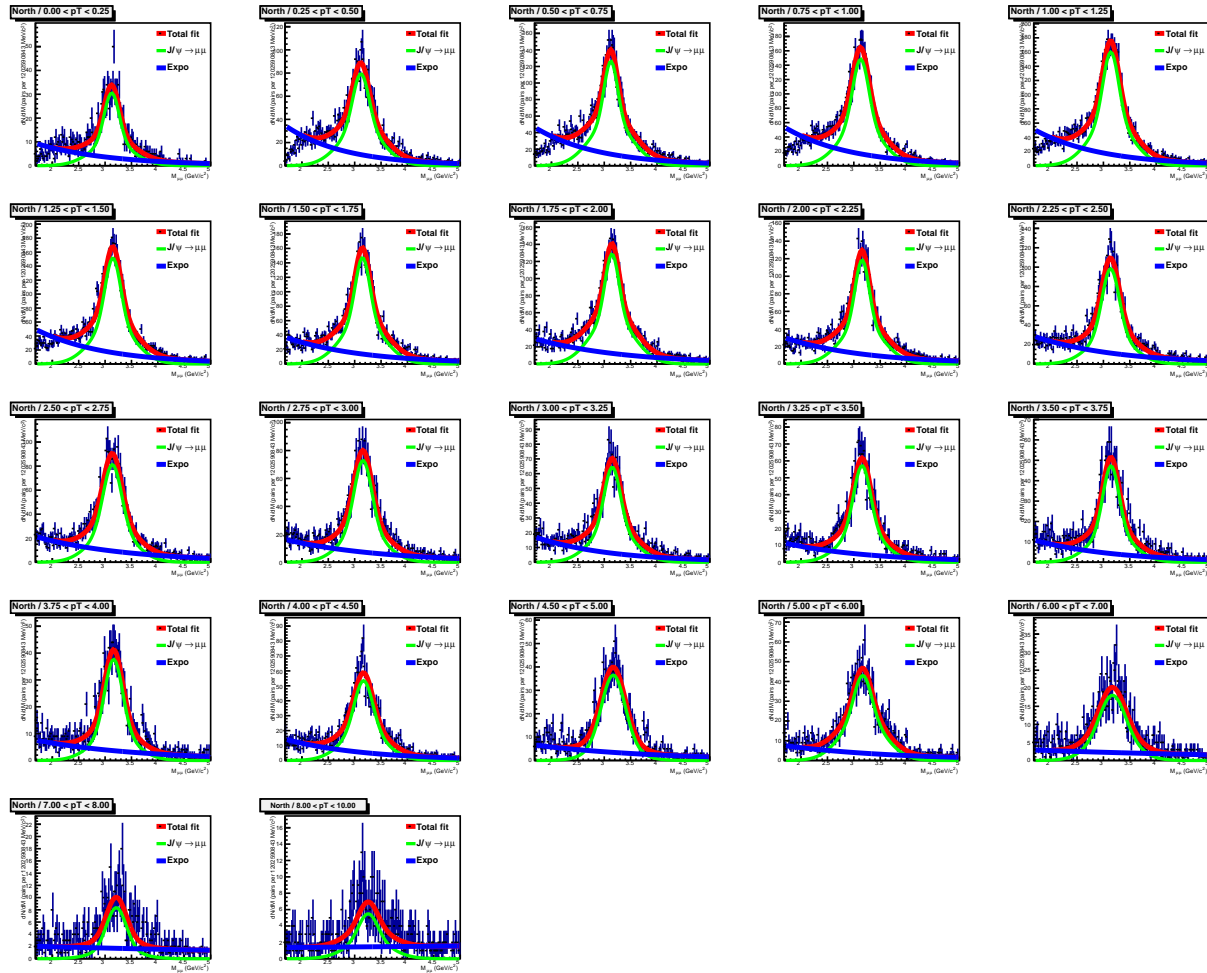


Figure 18: Unlike-sign mass spectra in the north arm fitted with Equation 3 showing J/ψ (green line) and correlated background (blue line) contributions for the north arm sorted in p_T .

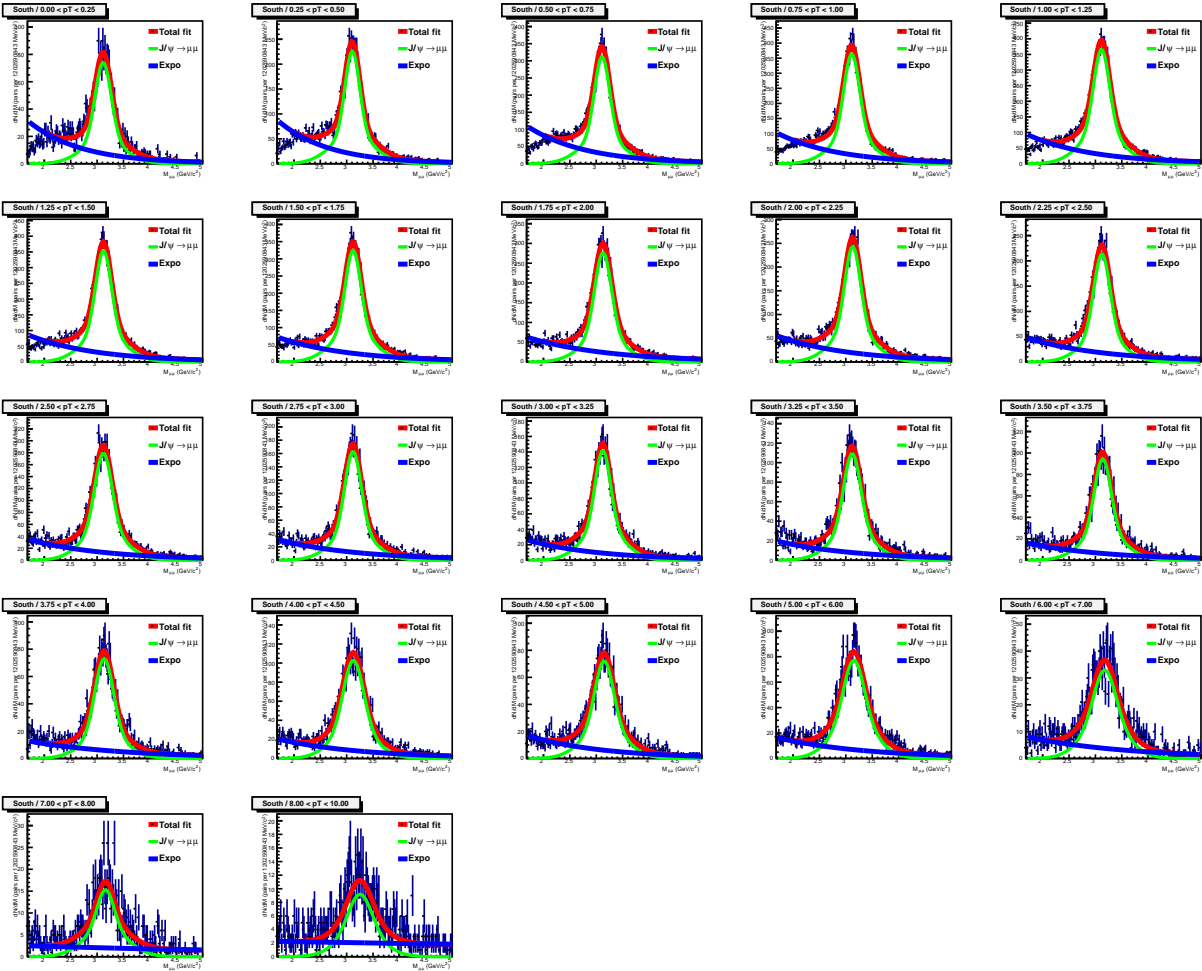


Figure 19: Unlike-sign mass spectra fitted with Equation 3 showing J/ψ (green line) and correlated background (blue line) contributions for the south arm sorted in p_T .

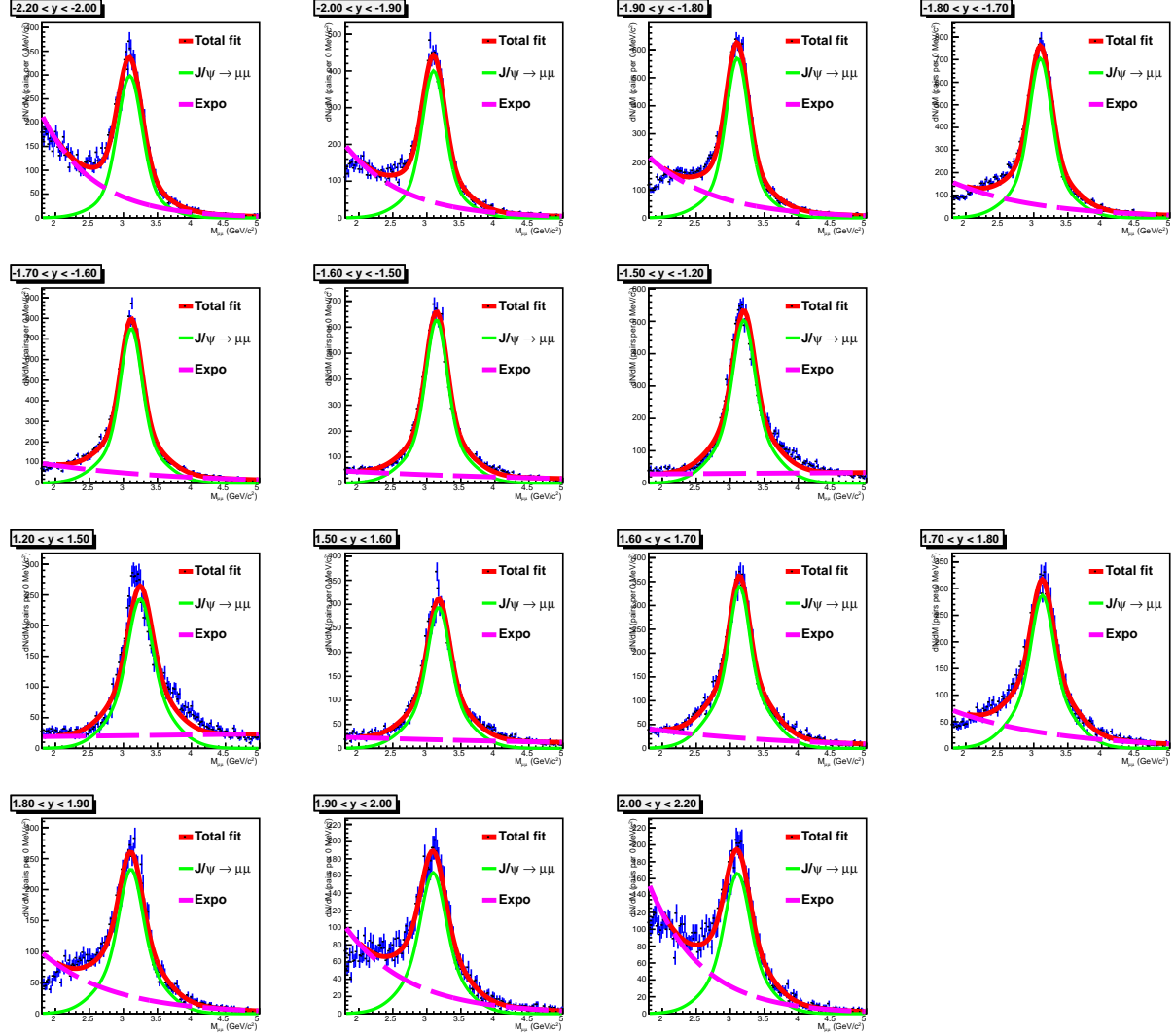


Figure 20: Unlike-sign mass spectra fitted with Equation 3 showing J/ψ (green line) and correlated background (blue line) contributions sorted in rapidity.

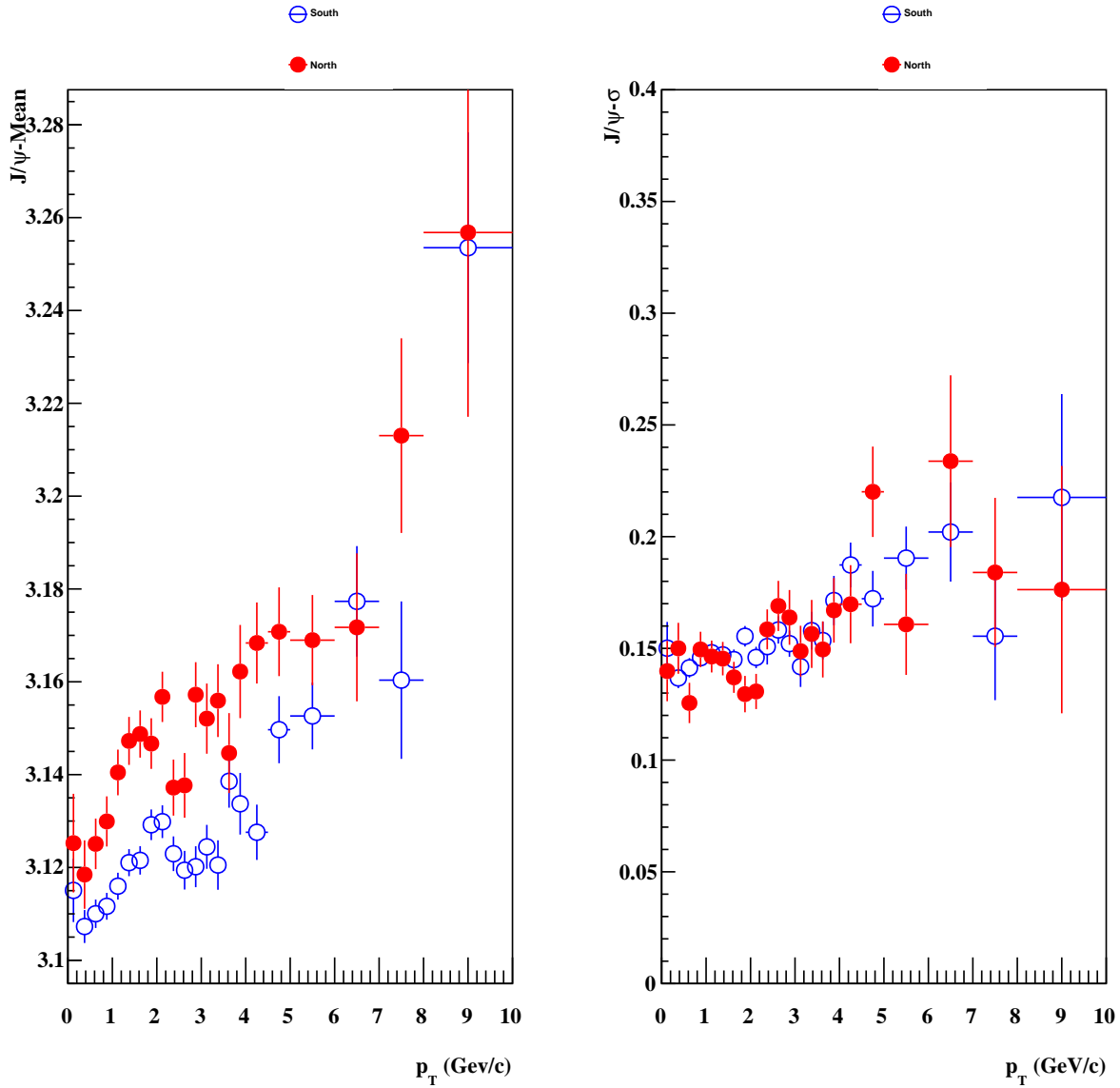


Figure 21: The mean (left) and width (right) for the north arm (solid red) and south arm (empty blue) from the p_T sorted unlike-sign mass spectra fitted with Equation 3.

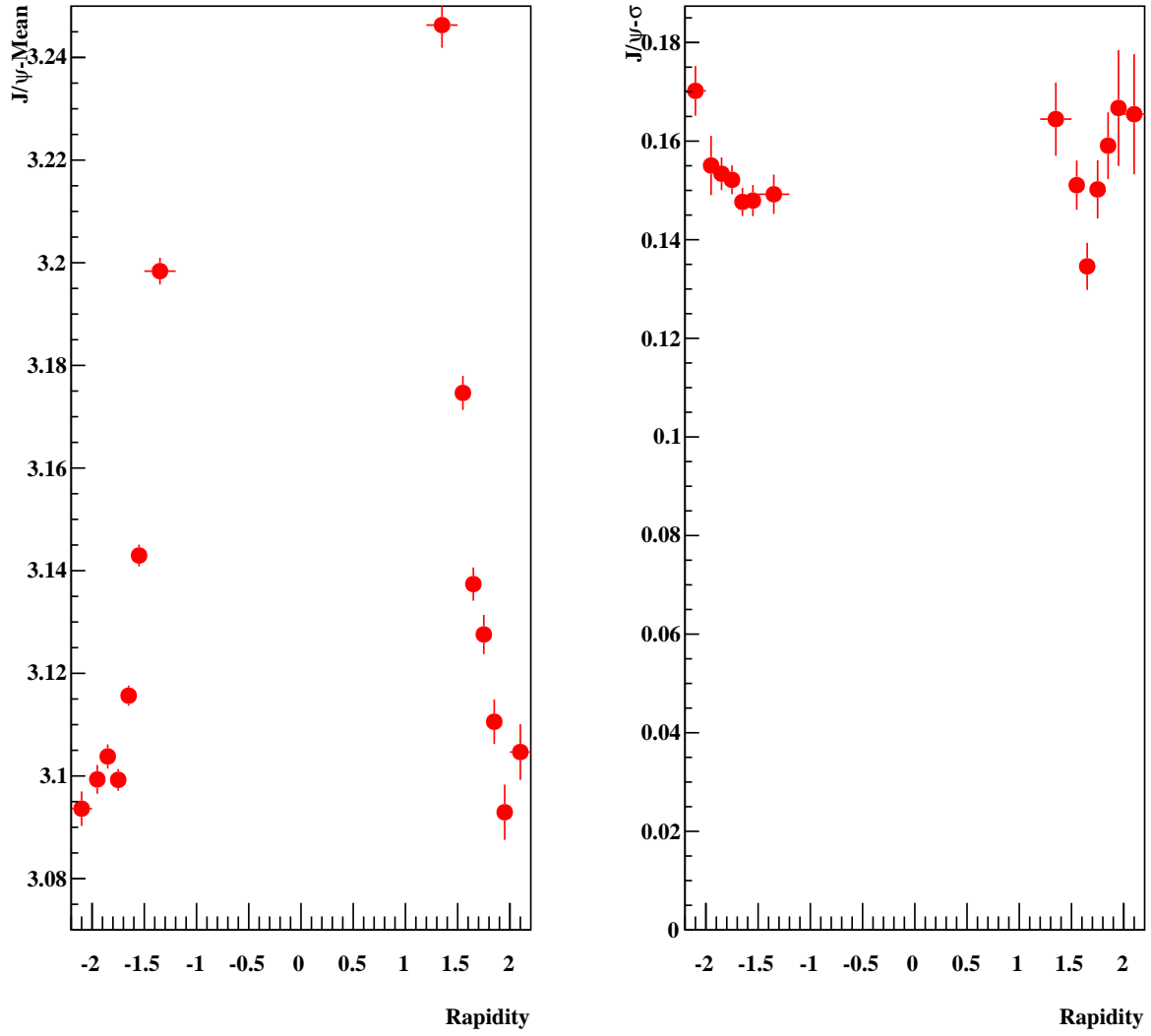


Figure 22: The mean (left) and width (right) from the rapidity sorted unlike-sign mass spectra fitted with Equation 3.

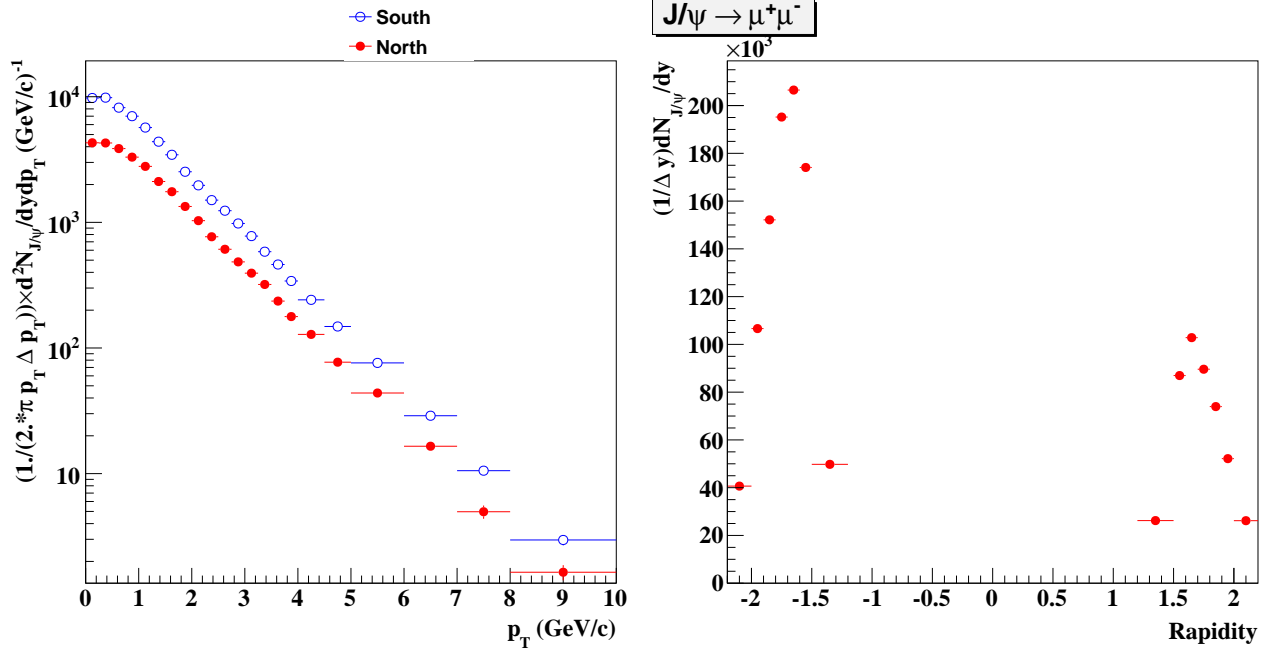


Figure 23: Left: J/ψ yields as a function of p_T for the north (solid red) and south (empty blue) arms. Right: J/ψ yields as a function of rapidity.

Table 4: J/ψ meson yield as a function of rapidity.

Rapidity	$N_{J/\psi}$ ($0 < p_T < 10$)
-2.20 - -2.00	$8.1e+03 \pm 1.4e+02$
-2.00 - -1.90	$1.1e+04 \pm 1.7e+02$
-1.90 - -1.80	$1.5e+04 \pm 1.7e+02$
-1.80 - -1.70	$2.0e+04 \pm 1.9e+02$
-1.70 - -1.60	$2.1e+04 \pm 1.8e+02$
-1.60 - -1.50	$1.7e+04 \pm 1.7e+02$
-1.50 - -1.20	$1.5e+04 \pm 1.6e+02$
1.20 - 1.50	$7.9e+03 \pm 1.2e+02$
1.50 - 1.60	$8.7e+03 \pm 1.2e+02$
1.60 - 1.70	$1.0e+04 \pm 1.3e+02$
1.70 - 1.80	$9.0e+03 \pm 1.3e+02$
1.80 - 1.90	$7.4e+03 \pm 1.2e+02$
1.90 - 2.00	$5.2e+03 \pm 1.3e+02$
2.00 - 2.20	$5.2e+03 \pm 1.4e+02$
Total	$1.6e+05 \pm 5.6e+02$

4 Acceptance and Reconstruction Efficiency

The acceptance and reconstruction efficiency, A_{rec} , of the muon spectrometers is determined by individually running PYTHIA, PHENIX's PYTHIA setup (PHPYTHIA), generated J/ψ through a full GEANT4 simulation of the PHENIX detector. PHPYTHIA was used to generate each J/ψ with a vertex distribution based on that of run13 BBC_z vertex (see left panel of Figure 24). Each set of events (5k) was tagged with

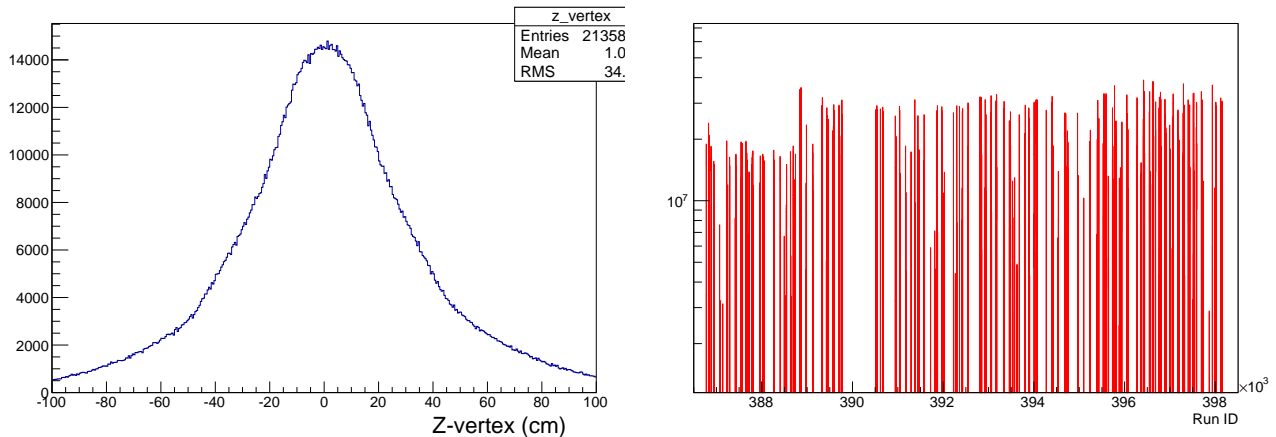


Figure 24: BBC_z vertex distribution (left panel) and MB triggers vs run ID (right panel) of all the runs used in the data analysis.

a run ID based on a 1D histogram of the MB triggers of the runs used in the data analysis (see right panel of Figure 24) and carried over to the stage of event reconstruction and embedding. This way the events are generated based on the rate and time distribution of the data and allows using the appropriate detector efficiencies and deadmaps as well as the embedding files matching the rate dependence of the data.

The exact PYTHIA control data card used for simulation is listed in appendix B. It should be mentioned that several k_T values were tested and no difference was observed until above 4 or more and so a $k_T \sim 2.1$ was chosen to be consistent with previous analyses. Figure 25 shows tuned p_T and rapidity distributions (based on those of PYTHIA), used as an input to the simulation such that the output p_T and rapidity distributions match those of the data.

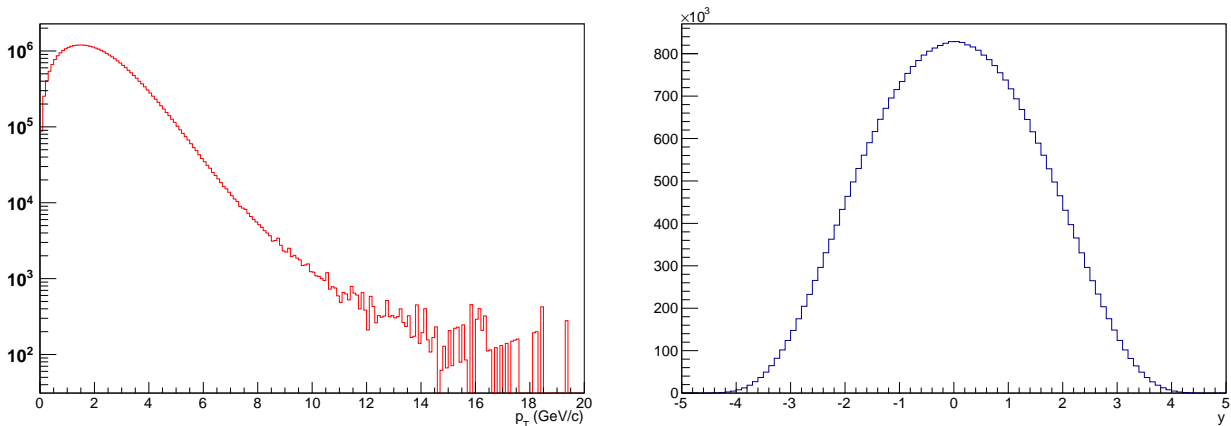


Figure 25: Tuned input p_T (left panel) and rapidity (right panel) distributions.

The generated events are then run through GEANT4 (run-13 510 GeV setup) and embedded into real $p+p$ data. For embedding we sampled one file from each of the runs used in the data analysis. For each set the run ID tag is used to call the associated embedding file. This also gives a reasonable description of the efficiencies and deadmaps for run13 collision rates.

To be consistent with the real data analysis, the same code that was used for the real data analysis was used for the simulation. The same data quality cuts were also used for the simulation. In addition, the trigger emulator tool (Tools::LL1 2D Decision) was used to match the dimuon live-trigger for the data. The efficiency of the trigger emulator was studied by applying it to the data and comparing the resulting mass spectrum to that of the dimuon live-trigger. The results (see Figure 26) show a difference of 1.5% (2.0%) in north (south) arms between the triggers.

To confirm the validity of the simulation, several distributions of the detector and tracking parameters were compared to the ones from the data, as shown in Figures 27 and 28 for the north and south arms, respectively, while Figures 29 and 30 show the same plots with linear scale. Note that the p_T distributions were plotted before the input p_T distributions were tuned. Figure 31 shows p_T distributions after the input p_T distributions were tuned.

To estimate $A\varepsilon_{rec}$, the J/ψ yield was extracted from the embedded MC simulation in a similar manner to that of the data. The dimuon mass spectra, in J/ψ region, was reconstructed for p_T and rapidity bins equivalent to those of the data and fitted with Equation 3, and the results are shown in Figures 32, 33, 34.

Figures 35 and 36 show the means and widths in the left and right panels, respectively, from these fits. The mean (mass) and the width (σ) of J/ψ mass distribution fits extracted from simulation were compared to those from the data, as shown in Figure 37.

The $A\varepsilon_{rec}$ was calculated by dividing the number of J/ψ 's extracted from the previous fits by the number of generated events in a given kinematic bin. The average $A\varepsilon_{rec}$ for unlike-sign pairs as a function of p_T and rapidity are shown in Figure 38. Tables 5 and 6 list the values of $A\varepsilon_{rec}$ as a function of p_T and rapidity, respectively.

Table 5: J/ψ meson $A\varepsilon_{rec}$ as a function of p_T for both south and north arms.

p_T (GeV/c)	$A\varepsilon_{rec}$ ($1.2 < y < 2.2$)	$A\varepsilon_{rec}$ ($-2.2 < y < -1.2$)
0.00 - 0.25	$1.3\text{e-}02 \pm 1.6\text{e-}04$	$2.8\text{e-}02 \pm 2.4\text{e-}04$
0.25 - 0.50	$1.3\text{e-}02 \pm 1.0\text{e-}04$	$2.9\text{e-}02 \pm 1.5\text{e-}04$
0.50 - 0.75	$1.3\text{e-}02 \pm 8.1\text{e-}05$	$2.8\text{e-}02 \pm 1.2\text{e-}04$
0.75 - 1.00	$1.3\text{e-}02 \pm 7.4\text{e-}05$	$2.8\text{e-}02 \pm 1.1\text{e-}04$
1.00 - 1.25	$1.3\text{e-}02 \pm 7.0\text{e-}05$	$2.7\text{e-}02 \pm 1.0\text{e-}04$
1.25 - 1.50	$1.3\text{e-}02 \pm 6.9\text{e-}05$	$2.6\text{e-}02 \pm 9.9\text{e-}05$
1.50 - 1.75	$1.3\text{e-}02 \pm 6.9\text{e-}05$	$2.5\text{e-}02 \pm 9.9\text{e-}05$
1.75 - 2.00	$1.3\text{e-}02 \pm 7.2\text{e-}05$	$2.5\text{e-}02 \pm 1.0\text{e-}04$
2.00 - 2.25	$1.3\text{e-}02 \pm 7.4\text{e-}05$	$2.4\text{e-}02 \pm 1.0\text{e-}04$
2.25 - 2.50	$1.4\text{e-}02 \pm 8.0\text{e-}05$	$2.6\text{e-}02 \pm 1.1\text{e-}04$
2.50 - 2.75	$1.5\text{e-}02 \pm 8.9\text{e-}05$	$2.7\text{e-}02 \pm 1.2\text{e-}04$
2.75 - 3.00	$1.5\text{e-}02 \pm 9.8\text{e-}05$	$2.8\text{e-}02 \pm 1.3\text{e-}04$
3.00 - 3.25	$1.6\text{e-}02 \pm 1.1\text{e-}04$	$3.0\text{e-}02 \pm 1.5\text{e-}04$
3.25 - 3.50	$1.7\text{e-}02 \pm 1.3\text{e-}04$	$3.1\text{e-}02 \pm 1.7\text{e-}04$
3.50 - 3.75	$1.8\text{e-}02 \pm 1.5\text{e-}04$	$3.3\text{e-}02 \pm 1.9\text{e-}04$
3.75 - 4.00	$1.9\text{e-}02 \pm 1.7\text{e-}04$	$3.3\text{e-}02 \pm 2.2\text{e-}04$
4.00 - 4.50	$2.0\text{e-}02 \pm 1.5\text{e-}04$	$3.6\text{e-}02 \pm 1.9\text{e-}04$
4.50 - 5.00	$2.3\text{e-}02 \pm 2.0\text{e-}04$	$4.0\text{e-}02 \pm 2.6\text{e-}04$
5.00 - 6.00	$2.7\text{e-}02 \pm 2.3\text{e-}04$	$4.5\text{e-}02 \pm 2.9\text{e-}04$
6.00 - 7.00	$3.3\text{e-}02 \pm 4.3\text{e-}04$	$5.6\text{e-}02 \pm 5.5\text{e-}04$
7.00 - 8.00	$3.9\text{e-}02 \pm 7.6\text{e-}04$	$6.8\text{e-}02 \pm 1.0\text{e-}03$
8.00 - 10.00	$4.7\text{e-}02 \pm 1.0\text{e-}03$	$8.0\text{e-}02 \pm 1.4\text{e-}03$

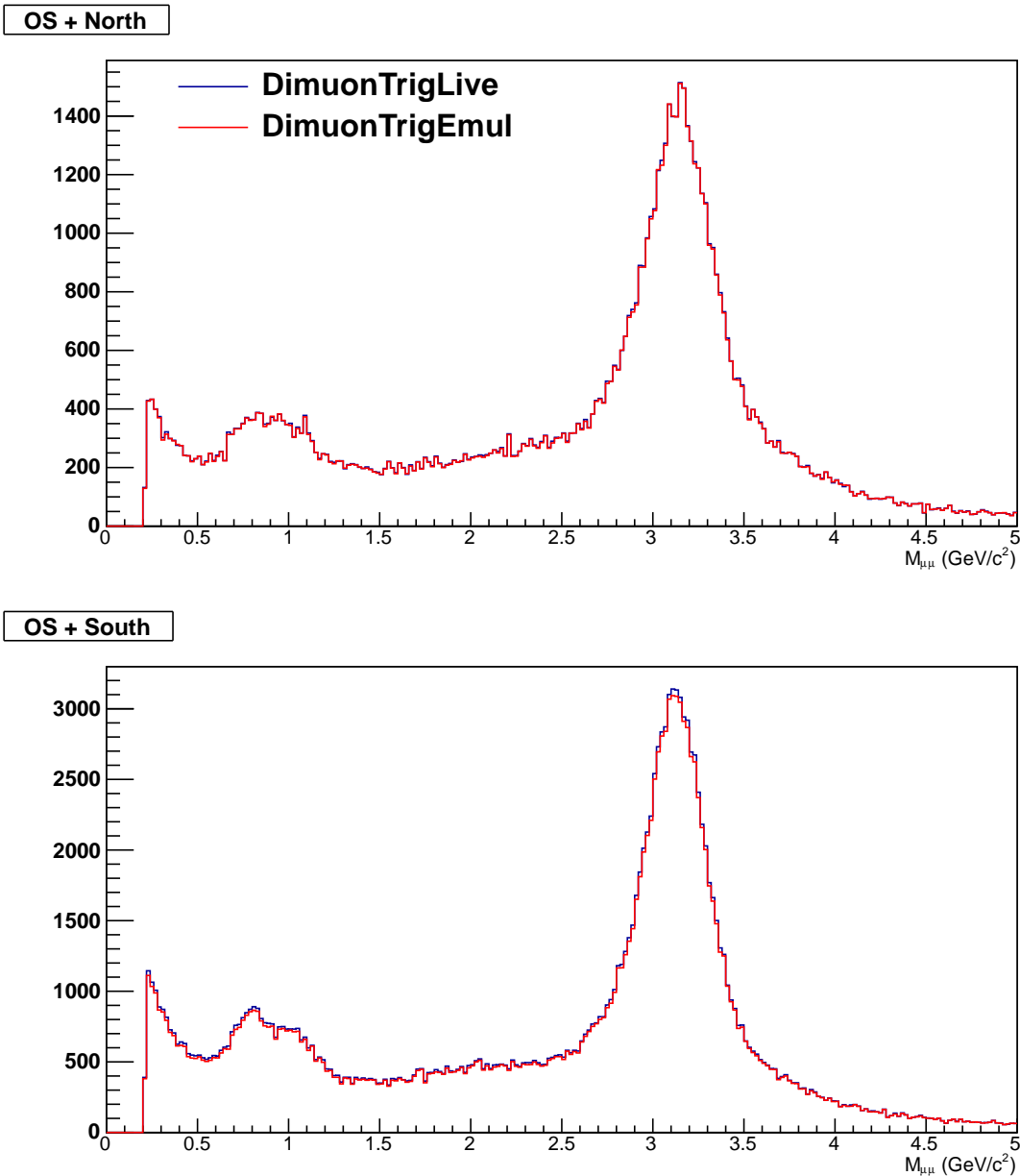


Figure 26: Dimuon mass distribution generated via the dimuon live-trigger (blue) and trigger emulator (red).

The systematic uncertainty associated with $A_{\epsilon_{rec}}$ includes the uncertainty on the input p_T and rapidity distributions which is extracted by varying these distributions over the range of the statistical uncertainty of the data, yielding 4.4% (5.0%) for the north (south) arm. Additional systematic effect was also considered to account for the difference between data and simulation using the azimuthal angle distribution. Figure 39 shows the azimuthal angle distribution for data and simulation in the north arm (left) and the south arm (right). The single track ϕ distributions are chosen as an estimate of the disagreement between the data and the simulation, in a similar fashion to analyses that were carried out in Ref. [13,14]. Due to the ambiguity about which octant to use for the normalization of the MC distribution each of the octants were chosen

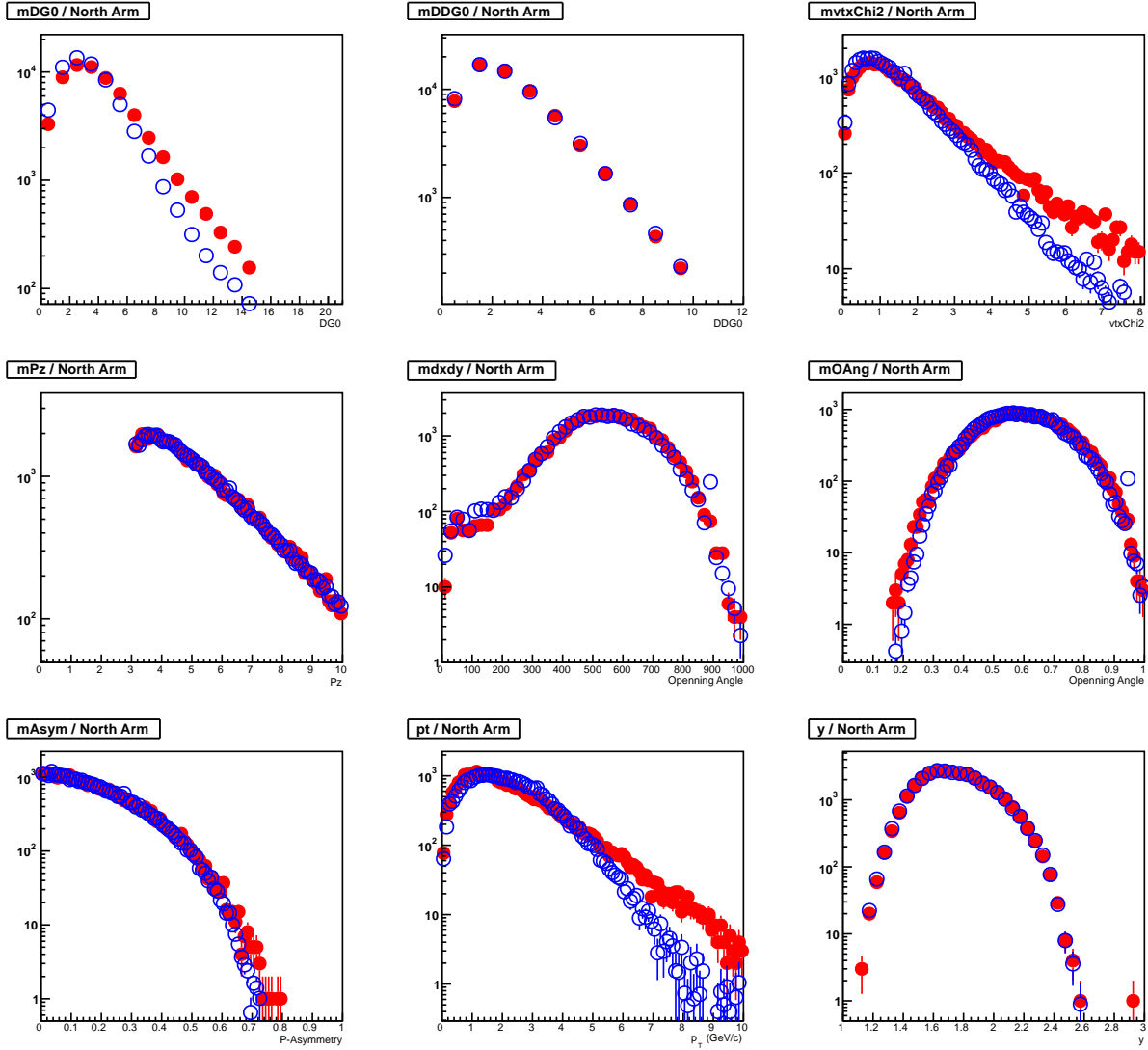


Figure 27: Comparison between data (solid red) and simulation (empty blue) for several variables in the north arm.

individually to calculate a normalization factor ($R = N_{Data}/N_{MC}$), N_{Data} and N_{MC} are the yields from the data and simulation, respectively, for a particular octant, while using the rest of the octants to calculate RMS , according to the following:

$$RMS_i = \sqrt{\frac{1}{8-1} \sum_{j \neq i}^8 \left(\frac{N_{MC}^j R_i - N_{DATA}^j}{N_{MC}^j R_i} \right)^2} \quad (4)$$

Then, the results are weight averaged over all eight octants. This procedure resulted in a 11.2% for the north arm and 8.8% for the south arm.

The total systematic uncertainty associated with $A_{\epsilon_{rec}}$ is the sum of the three effects mentioned above and amounts to 12.1% for the north arm and 10.3% for the south arm.

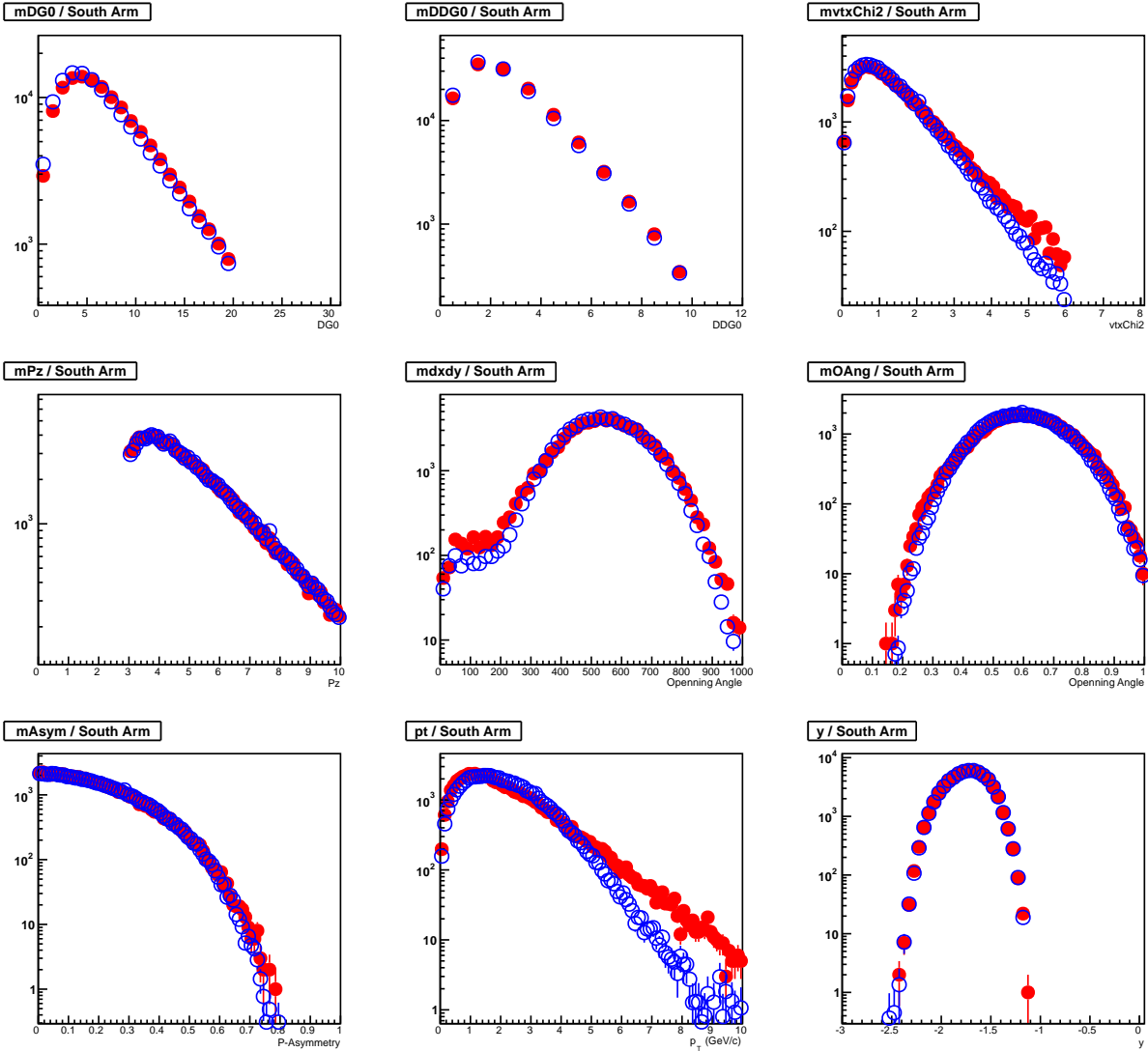


Figure 28: Comparison between data (solid red) and simulation (empty blue) for several variables in the south arm.

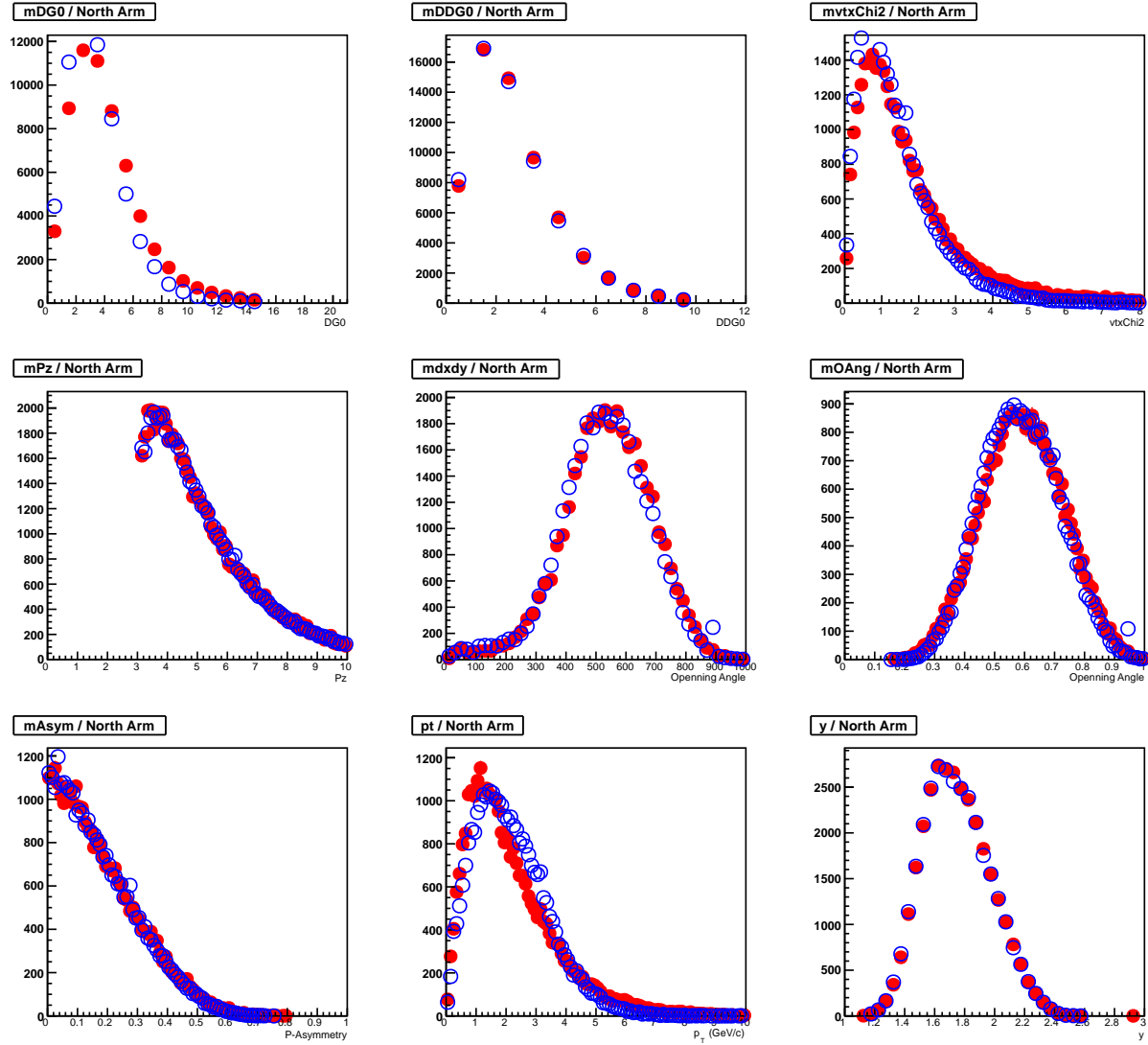


Figure 29: Comparison between data (solid red) and simulation (empty blue) for several variables in the north arm.

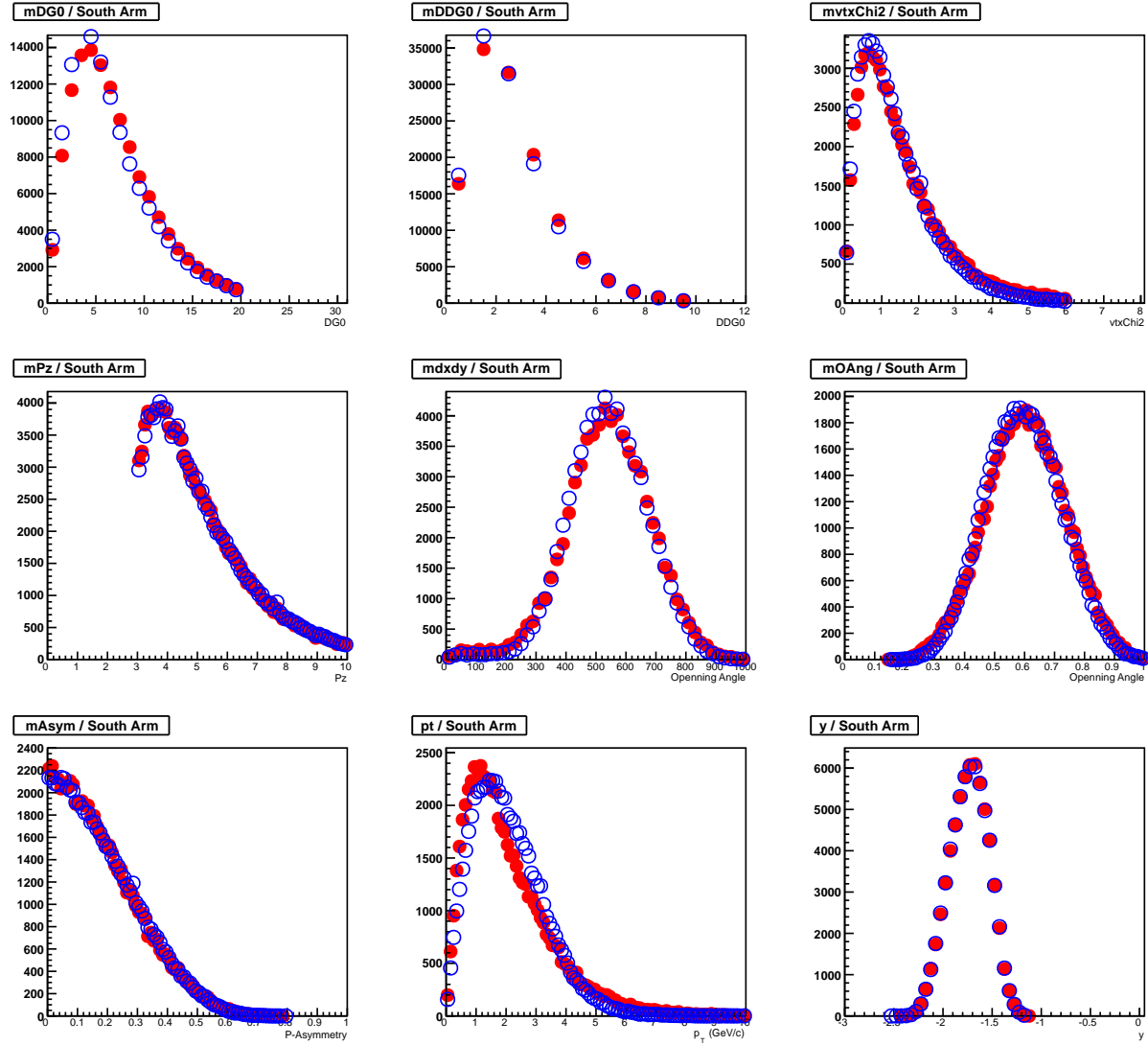


Figure 30: Comparison between data (solid red) and simulation (empty blue) for several variables in the south arm.

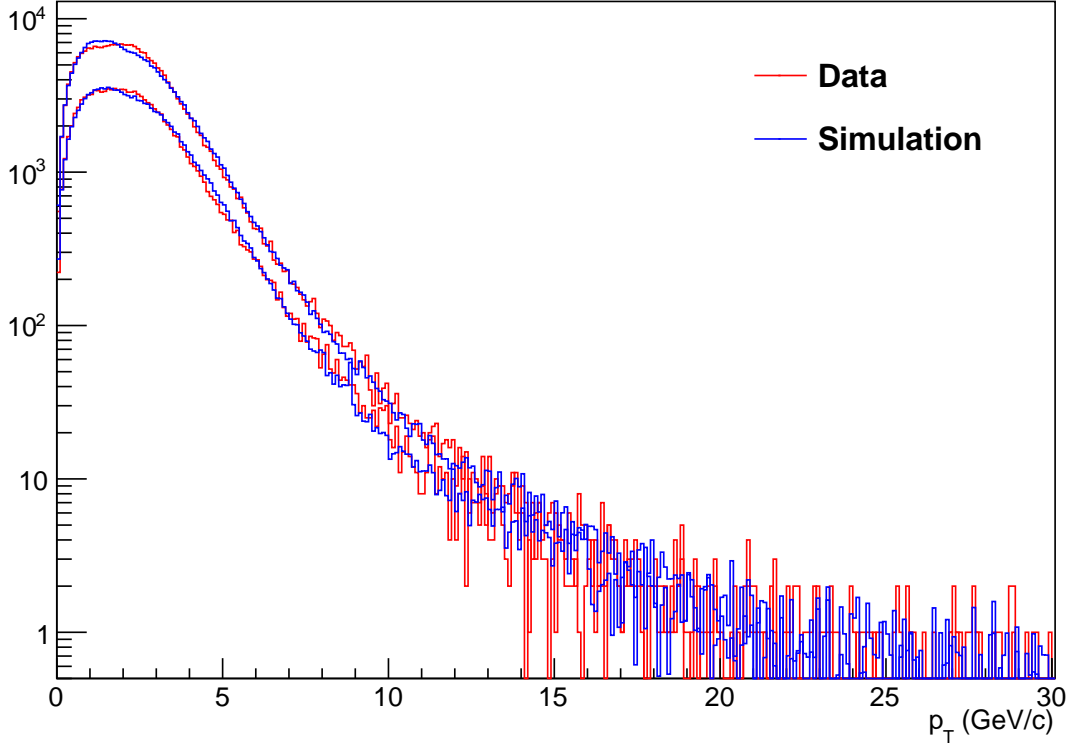


Figure 31: Output p_T distributions from the simulation compared to those of the data for the north (lower) and south (upper) arms.

Table 6: J/ψ meson $A\varepsilon_{rec}$ as a function of rapidity.

Rapidity	$A\varepsilon_{rec}$
-2.20 - -2.00	$2.2e-02 \pm 6.5e-05$
-2.00 - -1.90	$4.2e-02 \pm 1.3e-04$
-1.90 - -1.80	$4.8e-02 \pm 1.3e-04$
-1.80 - -1.70	$5.0e-02 \pm 1.3e-04$
-1.70 - -1.60	$4.7e-02 \pm 1.2e-04$
-1.60 - -1.50	$3.6e-02 \pm 1.1e-04$
-1.50 - -1.20	$9.6e-03 \pm 3.2e-05$
1.20 - 1.50	$5.4e-03 \pm 2.5e-05$
1.50 - 1.60	$1.9e-02 \pm 7.8e-05$
1.60 - 1.70	$2.3e-02 \pm 8.7e-05$
1.70 - 1.80	$2.5e-02 \pm 9.2e-05$
1.80 - 1.90	$2.3e-02 \pm 8.7e-05$
1.90 - 2.00	$2.0e-02 \pm 8.0e-05$
2.00 - 2.20	$1.4e-02 \pm 4.7e-05$

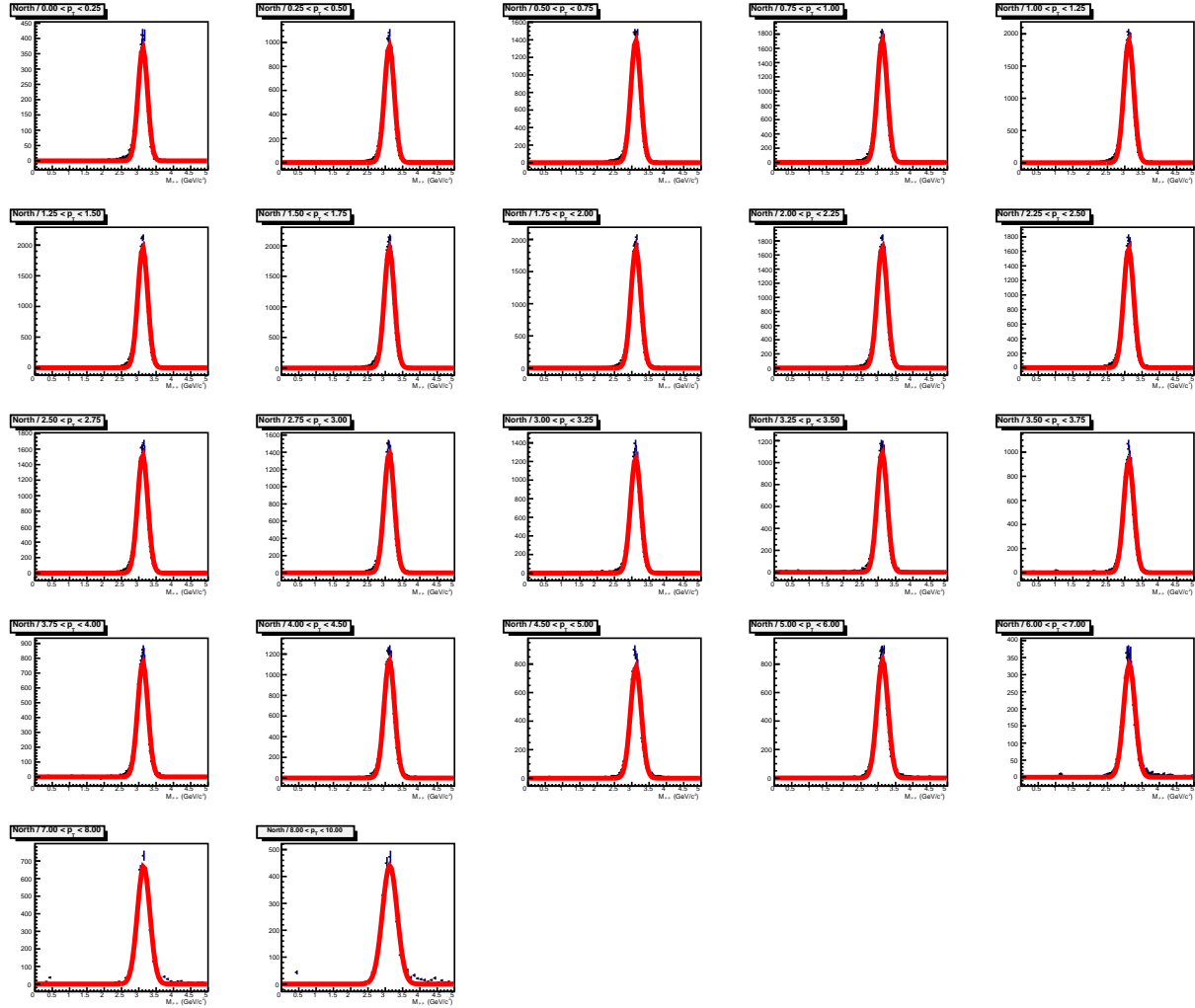


Figure 32: Simulation generated unlike-sign mass spectra in the north arm after subtracting the like-sign fitted with Equation 3.

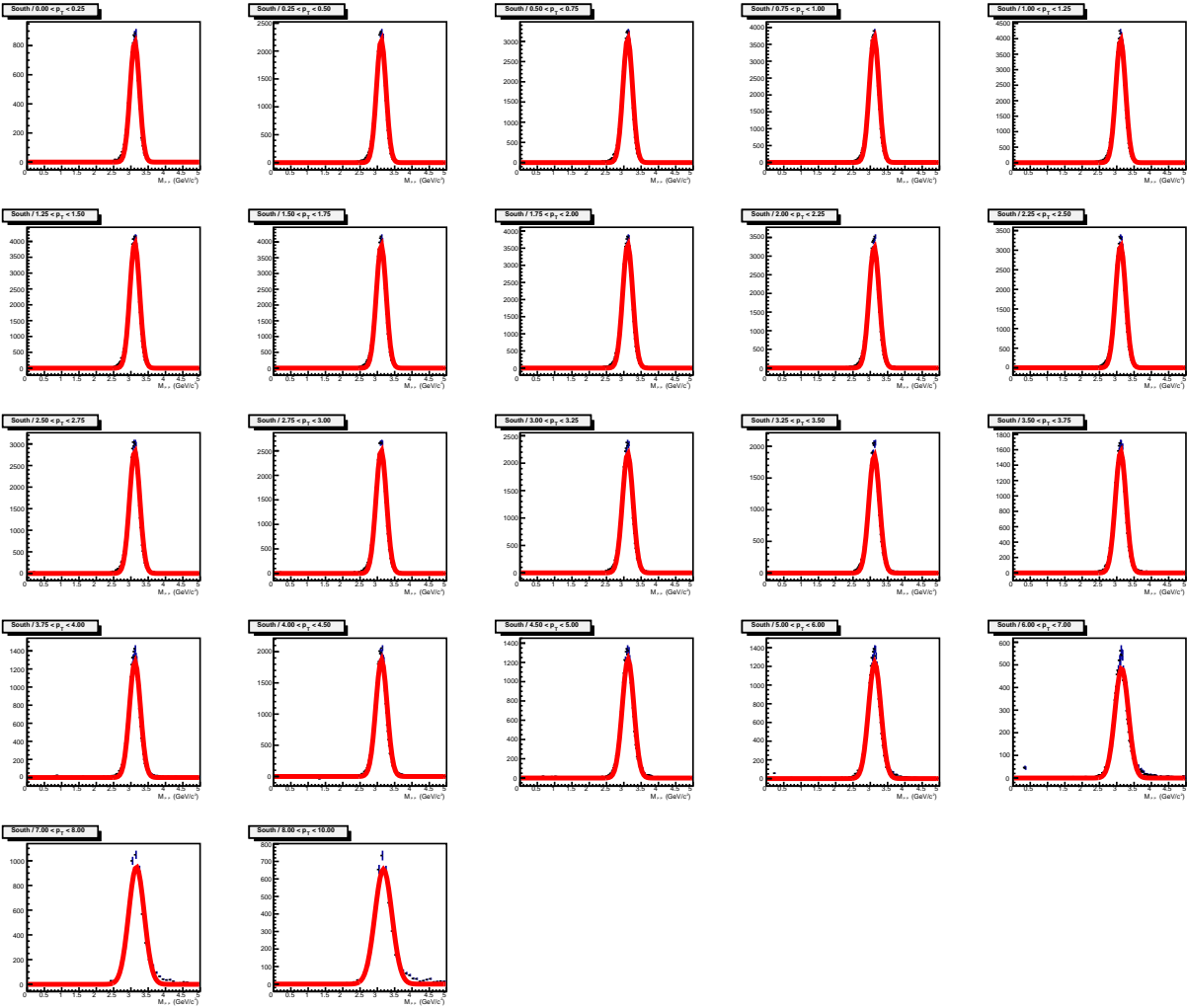


Figure 33: Simulation generated unlike-sign mass spectra in the south arm after subtracting the like-sign fitted with Equation 3.

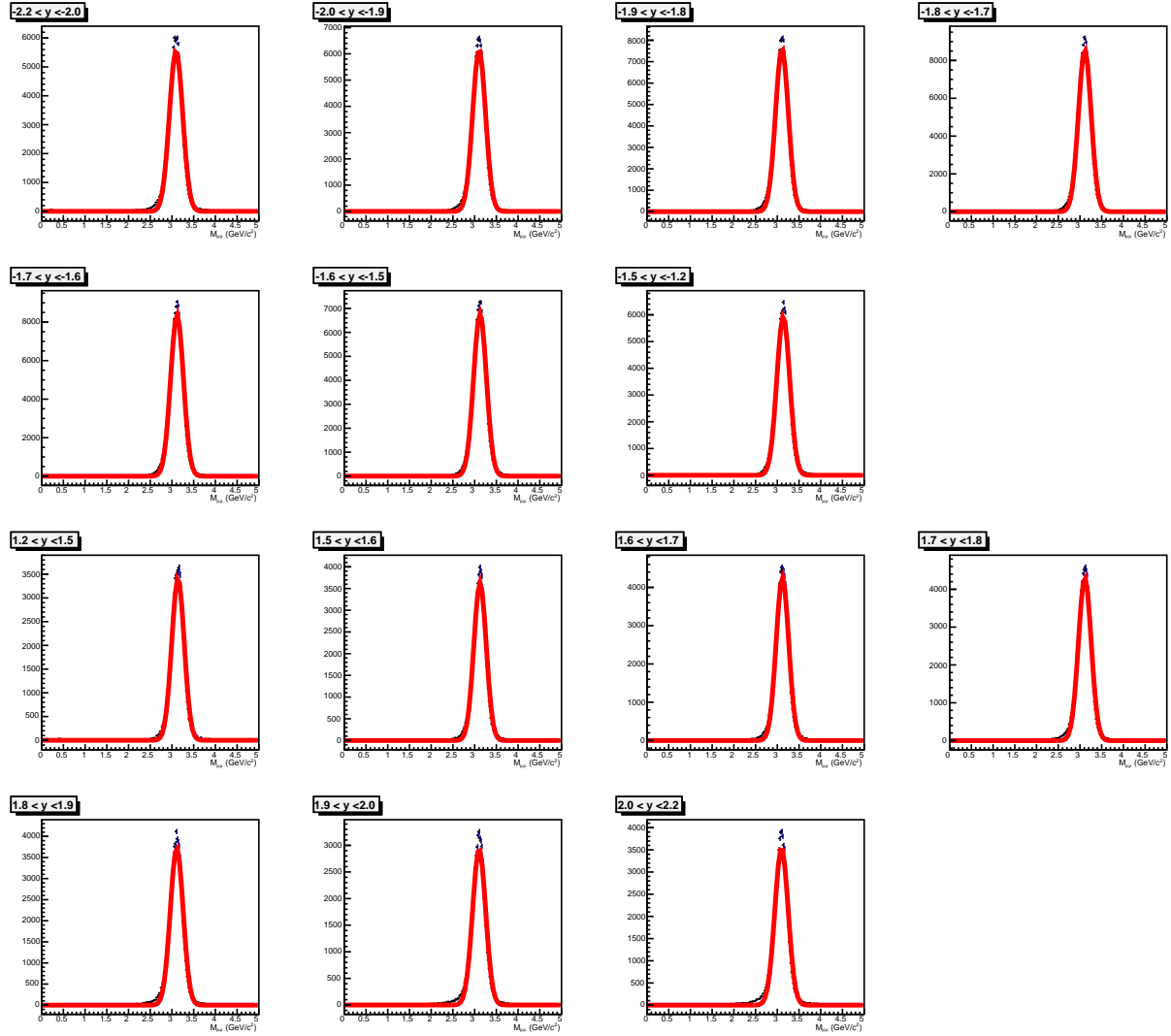


Figure 34: Simulation generated unlike-sign mass spectra after subtracting the like-sign fitted with Equation 3.

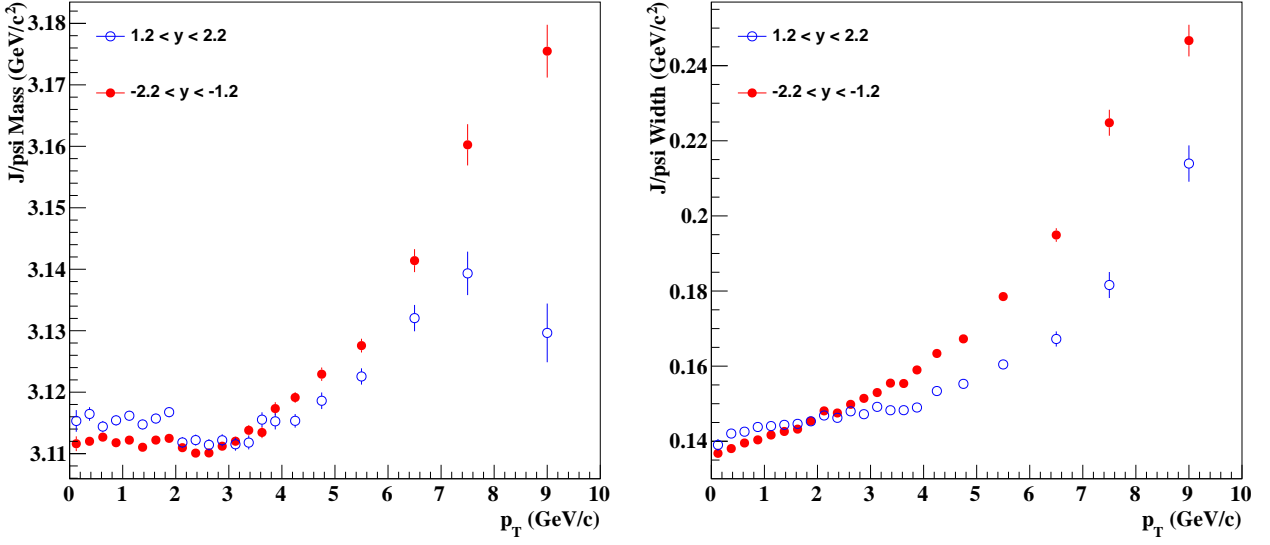


Figure 35: The mean (left) and width (right) from the p_T sorted unlike-sign mass spectra fitted with Equation 3.

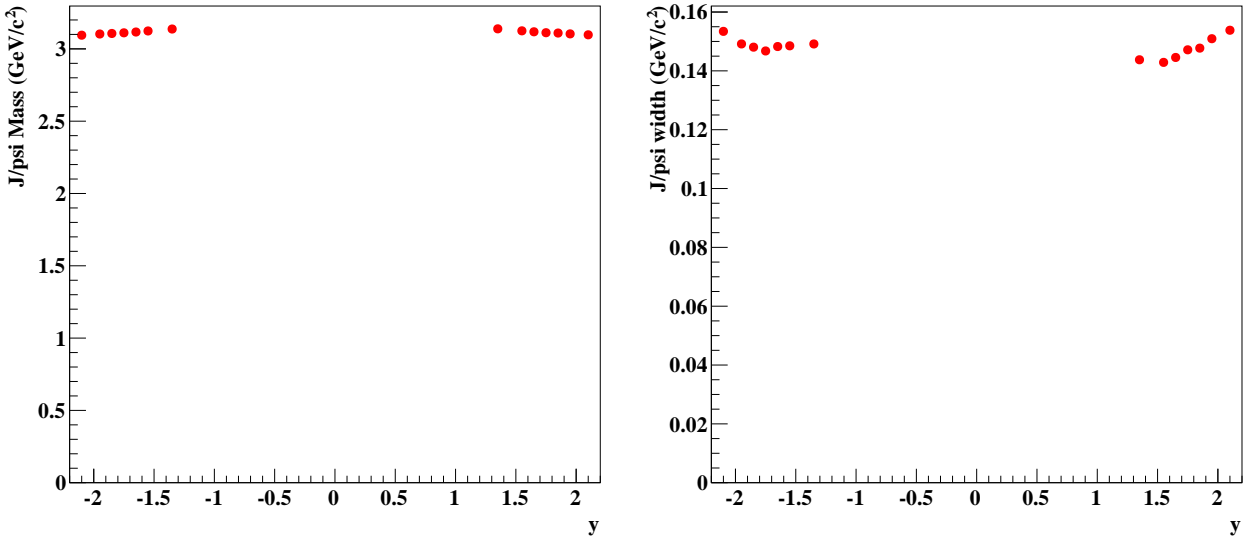


Figure 36: The mean (left) and width (right) from the rapidity sorted unlike-sign mass spectra fitted with Equation 3.

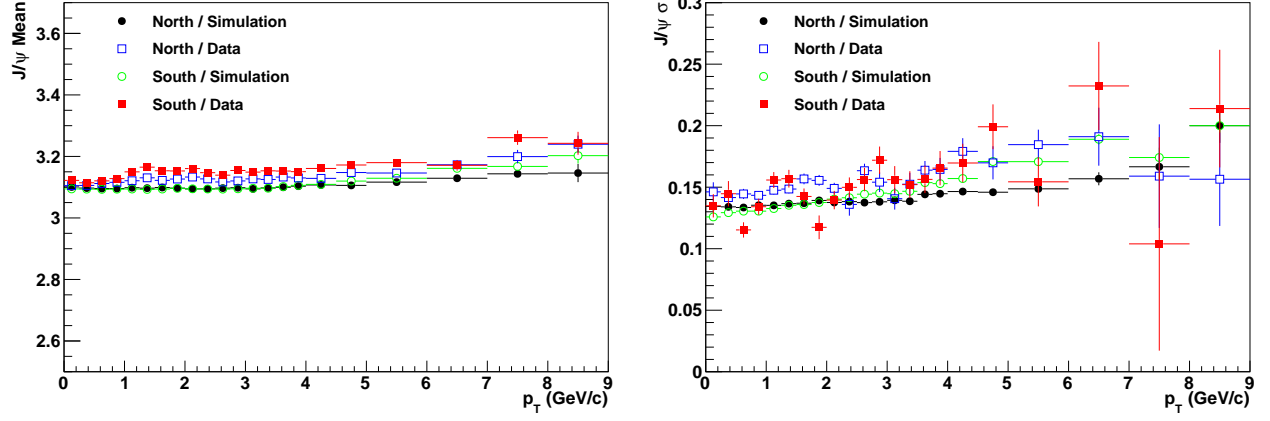
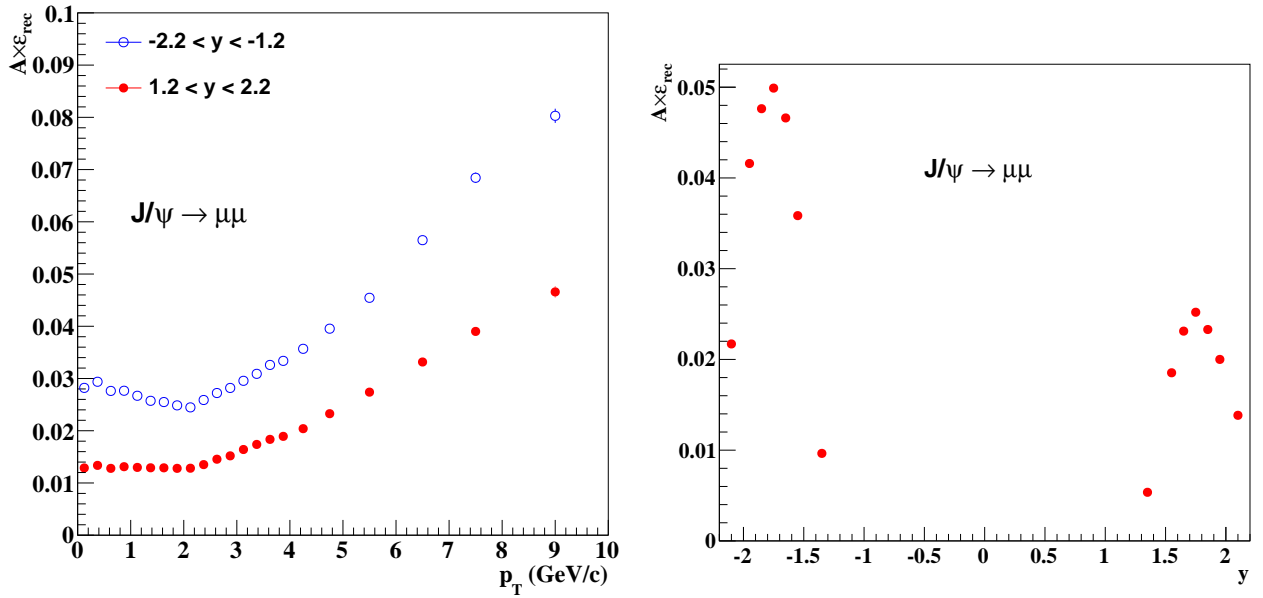


Figure 37: The mean (left) and width (right) from the simulation and compared to those from data.

Figure 38: J/ψ meson $A\epsilon_{rec}$ as a function of p_T (left) and as a function of rapidity (right).

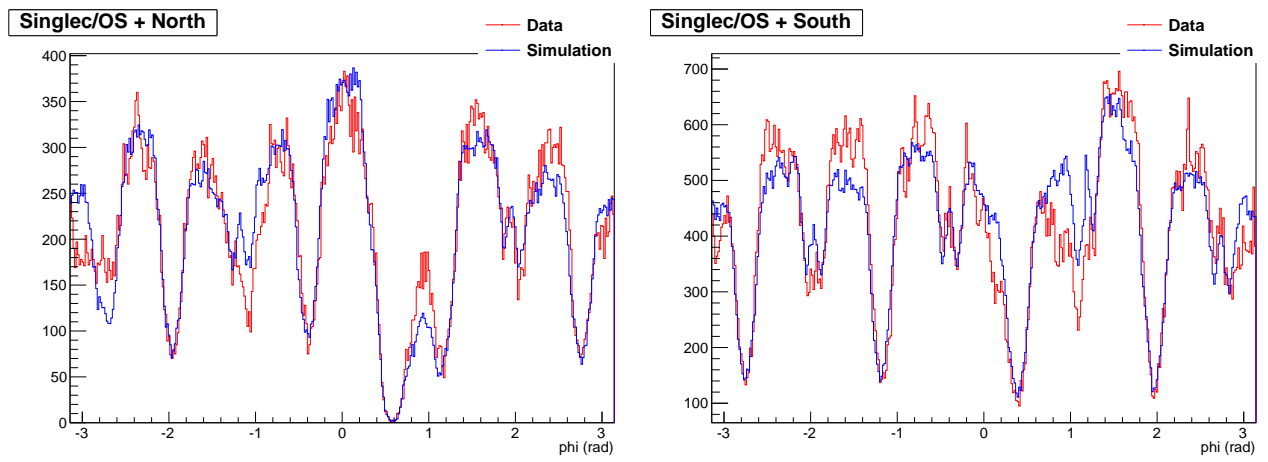


Figure 39: Single track ϕ distributions comparison between data (red) and simulation (blue) for the north arm (left) and the south arm (right).

To determine the effect of the cuts used in this analysis (listed in Table 2), we looked at the $A\varepsilon_{rec}$ distribution as a function p_T and rapidity without applying any cuts and monitored how the $A\varepsilon_{rec}$ changed as we add the cuts one by one. Figure 40 shows the $A\varepsilon_{rec}$ as a function of p_T for the studied cases while Figure 41 shows similar comparison for the $A\varepsilon_{rec}$ as a function of rapidity. The p_z cut has the most impact,

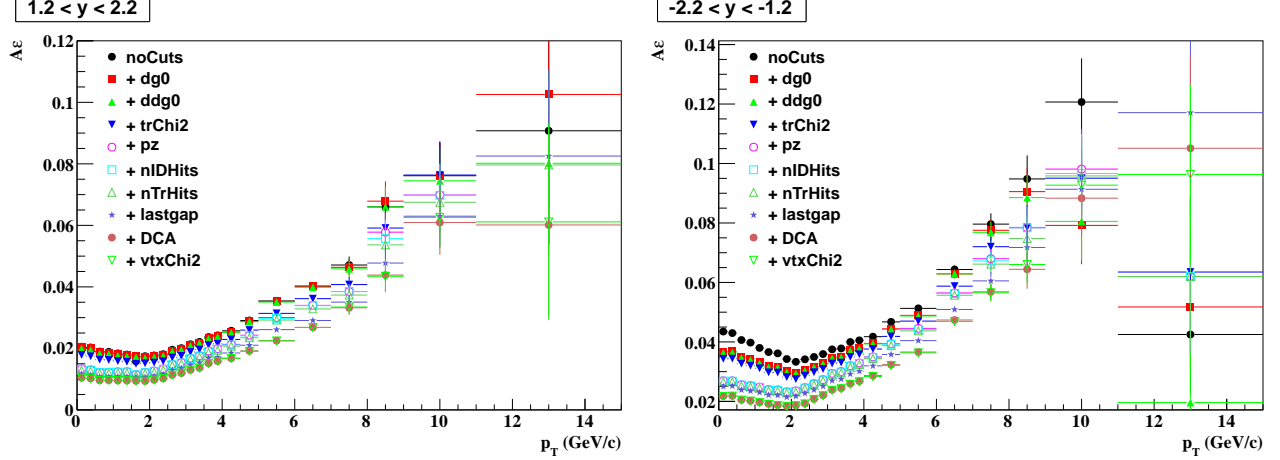


Figure 40: $A\varepsilon_{rec}$ as a function of p_T for the north arm (left) and south arm (right).

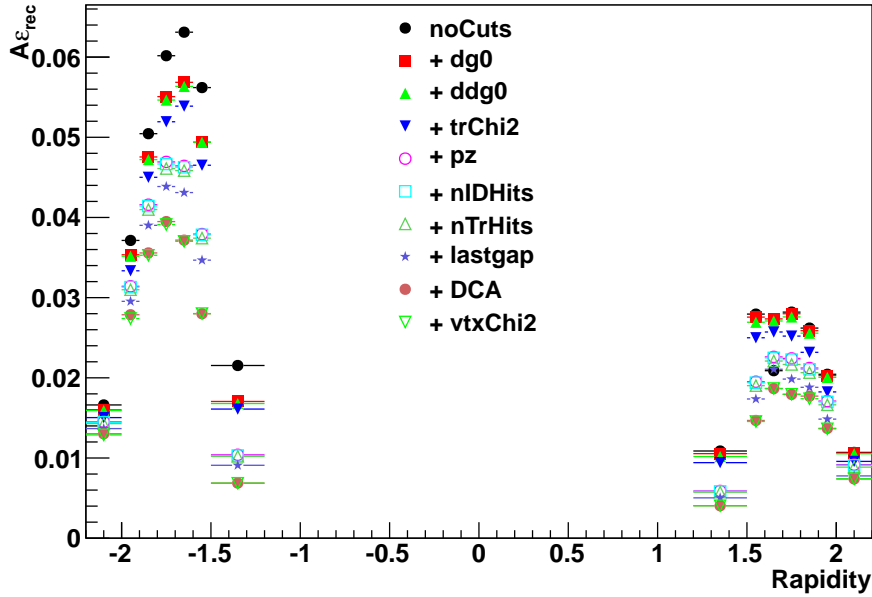


Figure 41: $A\varepsilon_{rec}$ as a function of rapidity.

however, this cut is set by the amount of absorber in front of the MuTr, which amounts to more than 3.0 GeV/c.

4.1 MuTr hit efficiency

The MuTr hit efficiency was the major issue that delayed the second for more than a year and a half. It was estimated by Sanghwa AN1327 [10] where she applied the base efficiency individually for each plane by using the plane by plane hit efficiency. The plane by plane hit efficiency was obtained as a function of the mean collision rate by looking at the hitmap. The work was done for the W analysis and may not be appropriate for lower p_T analysis such as this. Additional issue was that the MuTr deadmaps were included in this calculations and it not clear to what extent we will have double counting if we use MuTr deadmaps while at the same time apply the MuTr hit efficiency. Sanghwa's calibration implicitly uses MuTr tracking pattern recognition to restrict the calibration to a portion of acceptance, within which efficiency in multiple MuTr planes are high enough so that the tracks can be found. This definition of hit efficiency is partially aware of (not duplicating) some databased dead area (e.g. in case where a relatively thick stack of planes are known to be dead) but not likely for some other scenarios (i.e. duplicating dead area in database, e.g. for the known single plane dead area). This suggest that, in either the cases of using or not using the database deadmap in the simulation, it is not entirely right, which leads to a systematic uncertainty. Jin Haung's suggestion to deal with this problem was the following:

Use the best MuTr deadmap in simulation, to account for known dead areas similar to other MuTr analysis. In addition, use a rate-dependent MuTr hit efficiency that is based on Sanghwa's study, but redefined it to capture the rate-dependent effect only

$$Eff_{rate_dependent}(\mu) = Eff_{Sanghwa}(\mu) / Eff_{Sanghwa}(\mu = 0.15) * 0.98(\text{default hit efficiency in sim.}) \quad (5)$$

This force the rate dependent portion of the efficiency = 100% for $\mu @ 0.15$, the lowest luminosity in Sanghwa's calibration dataset.

This procedure under count rate dependent efficiency effect by assuming rate dependent efficiency = 100% between $\mu = 0.15$ and only count this effect beyond $\mu > 0.15$. Related to the above point, the base efficiency at $\mu = 0$ was assumed to be 98% in the known alive area.

Following this procedure, I obtained much higher $A\varepsilon_{rec}$ than expected which made the differential cross section at 510 GeV lower than that at 200 GeV which pointed to a problem with this method. As Jin points in his email this is based on the assumption that the rate dependent efficiency = 100% at $\mu = 0.15$ which could be wrong. To further understand the effect, I carried to additional calculations: (1) Calculating

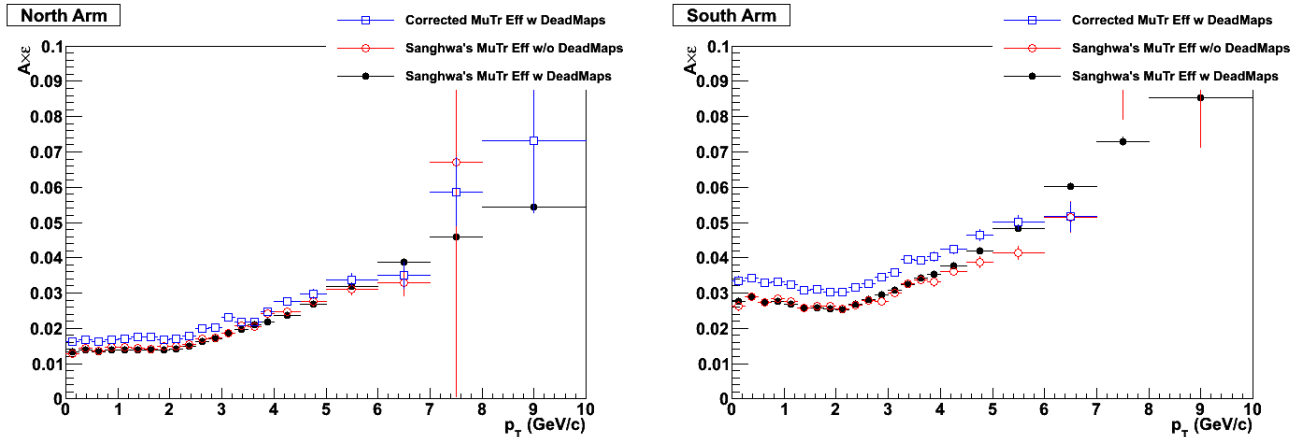


Figure 42: $A\varepsilon_{rec}$ comparison of the three methods listed in the text for north (left) and south (right).

$A\varepsilon_{rec}$ using Sanghwa's MuTr hit efficiency and applying MuTr deadmaps and (2) Calculating $A\varepsilon_{rec}$ using Sanghwa's MuTr hit efficiency according to the formula above and without applying MuTr deadmaps. If the method listed above is correct then the $A\varepsilon_{rec}$ using it should be below or near the one in (2) but above (1).

However, the results were very surprising; $A\varepsilon_{rec}$ in (2) was near but a little higher than (1) and much lower than the one with the corrected gains listed above, as shown in Figure 42.

This led to conclusion that the assumptions in the method with correct Sanghwa's hit efficiencies are not valid. Therefore, we decided to calculate $A\varepsilon_{rec}$ using (1) with Sanghwa's MuTr hit efficiency corrections and applying MuTr deadmaps and use the difference between (1) and (2) as systematic uncertainty on $A\varepsilon_{rec}$. This led to a systematic uncertainty of 8.2% (2.8%) in the north (south) arm.

5 Differential Cross Sections

The invariant yield and differential cross section are calculated according to the following relations:

$$\frac{1}{2\pi p_T} \frac{d^2 N}{dp_T dy} = \frac{1}{2\pi p_T} \frac{1}{B_{\mu^+\mu^-}} \frac{N_{J/\psi}(\Delta p_T)}{\Delta p_T \Delta y} \frac{1}{A\varepsilon(\Delta p_T)} \frac{1}{N_{MB}^{BBC}} \frac{\varepsilon_{MB}^{BBC}}{\varepsilon^{BBC}} \quad (6)$$

$$\frac{1}{2\pi p_T} \frac{d^2 \sigma}{dp_T dy} = \frac{1}{2\pi p_T} \frac{d^2 N}{dp_T dy} \sigma_{total} \quad (7)$$

$$\frac{dN}{dy} = \frac{1}{B_{\mu^+\mu^-}} \frac{N}{\Delta y} \frac{1}{A\varepsilon} \frac{1}{N_{MB}^{BBC}} \frac{\varepsilon_{MB}^{BBC}}{\varepsilon^{BBC}} \quad (8)$$

$$\frac{d\sigma}{dy} = \frac{dN}{dy} \sigma_{total} \quad (9)$$

$$\sigma_{total} = \sigma_{BBC} / \varepsilon_{MB}^{BBC} \quad (10)$$

where σ_{BBC} is the BBC cross section, $32.5 \pm 3.2\%$ mb, which is propagated from the Vernier scan result of Run9 [15]. ε_{MB}^{BBC} is MB efficiency, 0.53 ± 0.02 , and ε^{BBC} is the efficiency of MB trigger for events containing hard scattering, 0.91 ± 0.04 [9]. N_{MB}^{BBC} ($=2.95 \times 10^{12}$) is the number of MB events, and $N_{J/\psi}$ is the yield of J/ψ meson. The total number of MB events is multiplied by 1.025 to account for multiple collisions effect (see section ??). $A\varepsilon$ is the detector's acceptance and reconstruction efficiency (see section 4), and $B_{\mu^+\mu^-}$ is the branching ratio, where $B_{J/\psi \rightarrow \mu^+\mu^-} = 5.93 \pm 0.06\%$ [16]. $N_{MB}^{BBC} = 3.06 \times 10^{12}$ for the analyzed runs, however, there were several runs with muon 2D trigger scaled down, see appendix C, and need to account for that. This is done by dividing the BBCLL1 live trigger counts for those run by (scale+1), which gives $N_{MB}^{BBC} = 2.95 \times 10^{12}$. N_{MB}^{BBC} is also corrected for the multiple collisions effect, see section ??, which gives 3.02×10^{12} . It was also observed that the muon 2D trigger has a much lower livetime, $\sim 72.6\%$, than that of the BBCLL1 trigger at $\sim 91.6\%$. Figure 43 shows the livetime for the runs used in this analysis for the muon

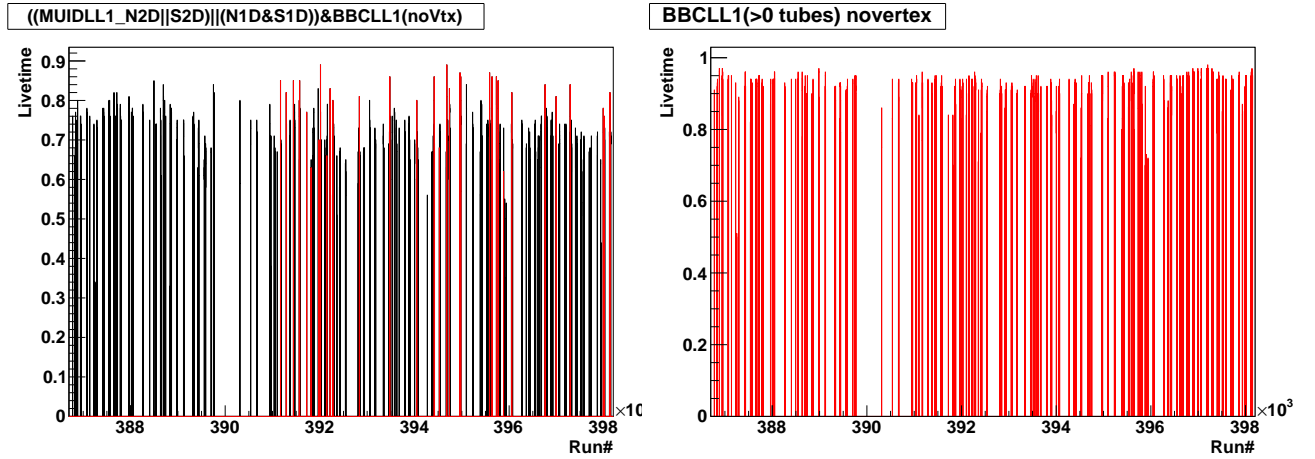


Figure 43: Livetime as a function of run number for ((MUIDLL1 N2D||S2D)||(N1D&S1D))&BBCLL1(noVtx) trigger (left) and for BBCLL1(>0 tubes) novertex (right). The prescaled runs are shown in red.

2D trigger in the left panel and for BBCLL1 trigger in the right panel. To account for this effect, the J/ψ yield is normalized by the ratio of the the muon 2D livetime (weighted by the muon 2D live trigger counts for the used runs), $\sim 72.6\%$, to that of the BBCLL1 livetime (weighted by the BBC live trigger counts for the used runs), $\sim 91.6\%$.

The J/ψ rapidity dependent differential cross section is shown in Figure 44.

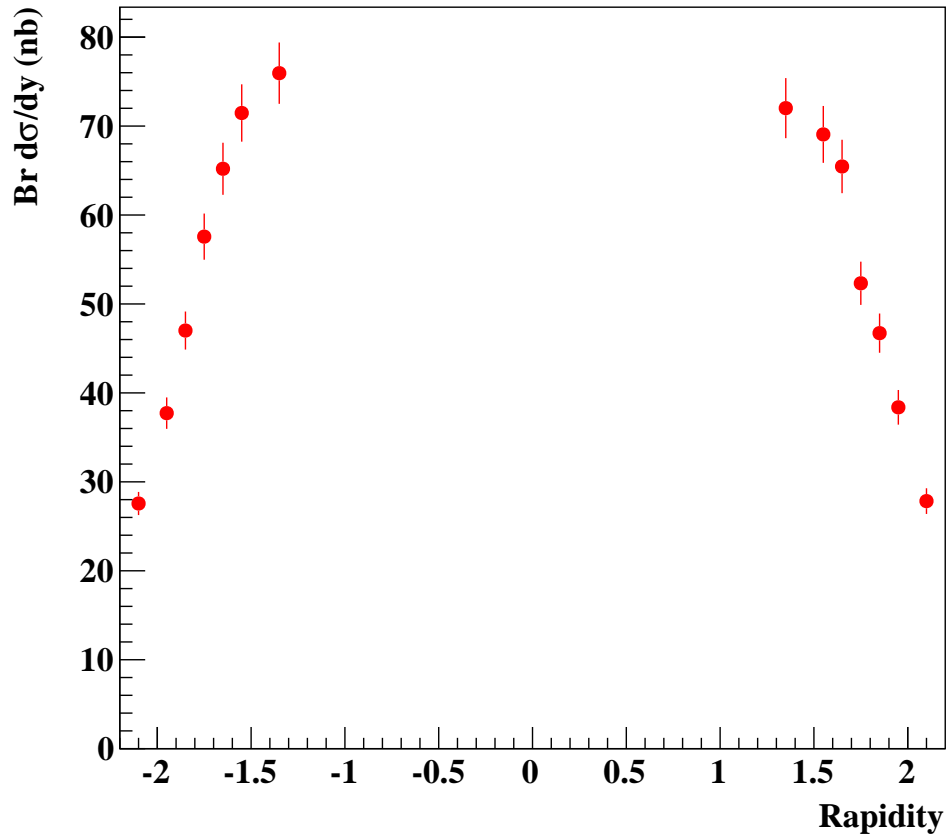


Figure 44: J/ψ differential cross section as a function of rapidity.

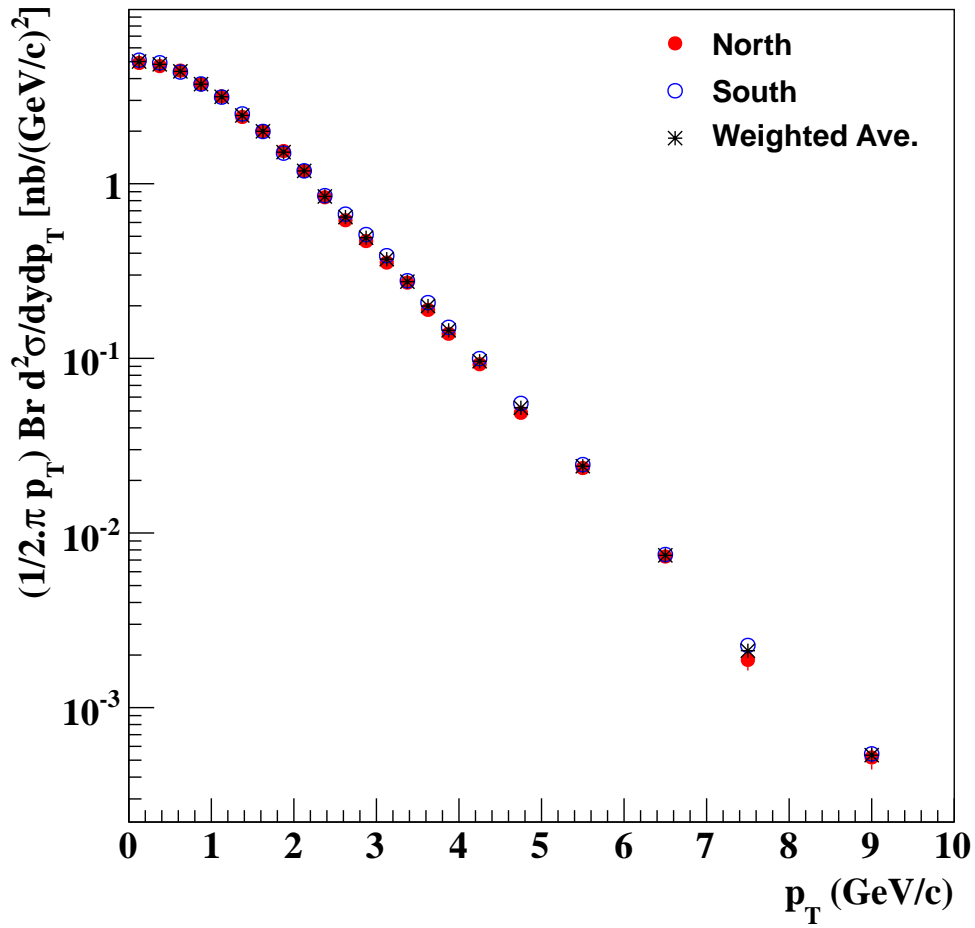


Figure 45: J/ψ differential cross sections as a function of p_T . The north arm is shown in solid red points, the south arm is shown in empty blue circles and the weighted average is shown in solid black stars.

The J/ψ p_T dependent differential cross sections in the north and south arms along with the weighted average are shown in Figure 45.

In extracting the p_T dependent cross section, the p_T distribution is divided into several p_T bins where each covers a finite range, however, the range gets very wide for higher p_T bins and given the steepness of the distribution it is necessary to determine the appropriate place to plot the data points. The appropriate place to plot the data point is determined by fitting the data points by a function, $f(p_T)$, and calculating the corrected value as $y_{corr.} = y_{uncorr.}/R$, where R [17] is,

$$R = \frac{1}{(p_T^{max} - p_T^{min}) \times f(p_T^{cent.})} \int_{p_T^{min}}^{p_T^{max}} f(p_T) dp_T \quad (11)$$

where $p_T^{cent.}$ is the center of the p_T bin. p_T^{min} and p_T^{max} are the minimum and maximum edges of the p_T bin. $f(p_T)$ is the Levy-Tsallis function [18]. Figure 46 shows J/ψ differential cross section as a function of

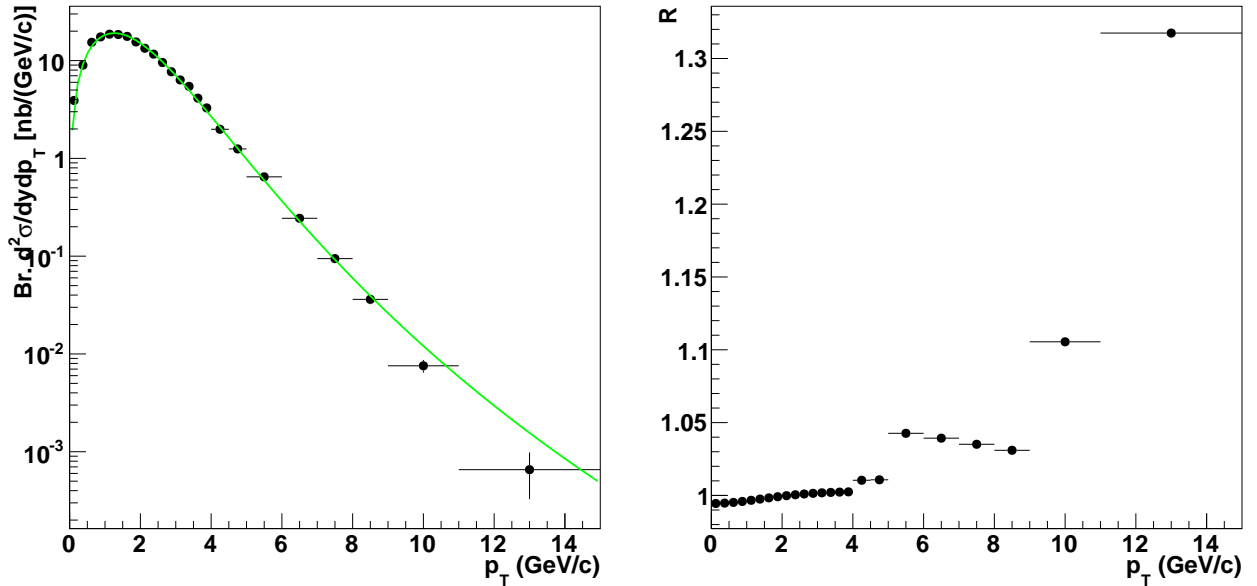


Figure 46: Left: J/ψ differential cross section as a function of p_T (solid black points) fitted by the Levy-Tsallis function [18] (green line). Right: The R factor as a function of p_T .

p_T fitted by the Levy-Tsallis function [18] in the left panel and the resulting R factor in the right panel and also listed in Table 7.

Figure 47 shows the corrected differential cross section averaged over the north and south arms.

Table 7: R factor as a function of p_T .

p_T (GeV/c)	R factor
0.000 - 0.250	$9.9\text{e-}01 \pm 9.9\text{e-}04$
0.250 - 0.500	$9.9\text{e-}01 \pm 9.9\text{e-}04$
0.500 - 0.750	$1.0\text{e+}00 \pm 1.0\text{e-}03$
0.750 - 1.000	$1.0\text{e+}00 \pm 1.0\text{e-}03$
1.000 - 1.250	$1.0\text{e+}00 \pm 1.0\text{e-}03$
1.250 - 1.500	$1.0\text{e+}00 \pm 1.0\text{e-}03$
1.500 - 1.750	$1.0\text{e+}00 \pm 1.0\text{e-}03$
1.750 - 2.000	$1.0\text{e+}00 \pm 1.0\text{e-}03$
2.000 - 2.250	$1.0\text{e+}00 \pm 1.0\text{e-}03$
2.250 - 2.500	$1.0\text{e+}00 \pm 1.0\text{e-}03$
2.500 - 2.750	$1.0\text{e+}00 \pm 1.0\text{e-}03$
2.750 - 3.000	$1.0\text{e+}00 \pm 1.0\text{e-}03$
3.000 - 3.250	$1.0\text{e+}00 \pm 1.0\text{e-}03$
3.250 - 3.500	$1.0\text{e+}00 \pm 1.0\text{e-}03$
3.500 - 3.750	$1.0\text{e+}00 \pm 1.0\text{e-}03$
3.750 - 4.000	$1.0\text{e+}00 \pm 1.0\text{e-}03$
4.000 - 4.500	$1.0\text{e+}00 \pm 1.0\text{e-}03$
4.500 - 5.000	$1.0\text{e+}00 \pm 1.0\text{e-}03$
5.000 - 6.000	$1.0\text{e+}00 \pm 1.0\text{e-}03$
6.000 - 7.000	$1.0\text{e+}00 \pm 1.0\text{e-}03$
7.000 - 8.000	$1.0\text{e+}00 \pm 1.0\text{e-}03$
8.000 - 9.000	$1.0\text{e+}00 \pm 1.0\text{e-}03$
9.000 - 11.000	$1.1\text{e+}00 \pm 1.1\text{e-}03$
11.000 - 15.000	$1.3\text{e+}00 \pm 1.3\text{e-}03$

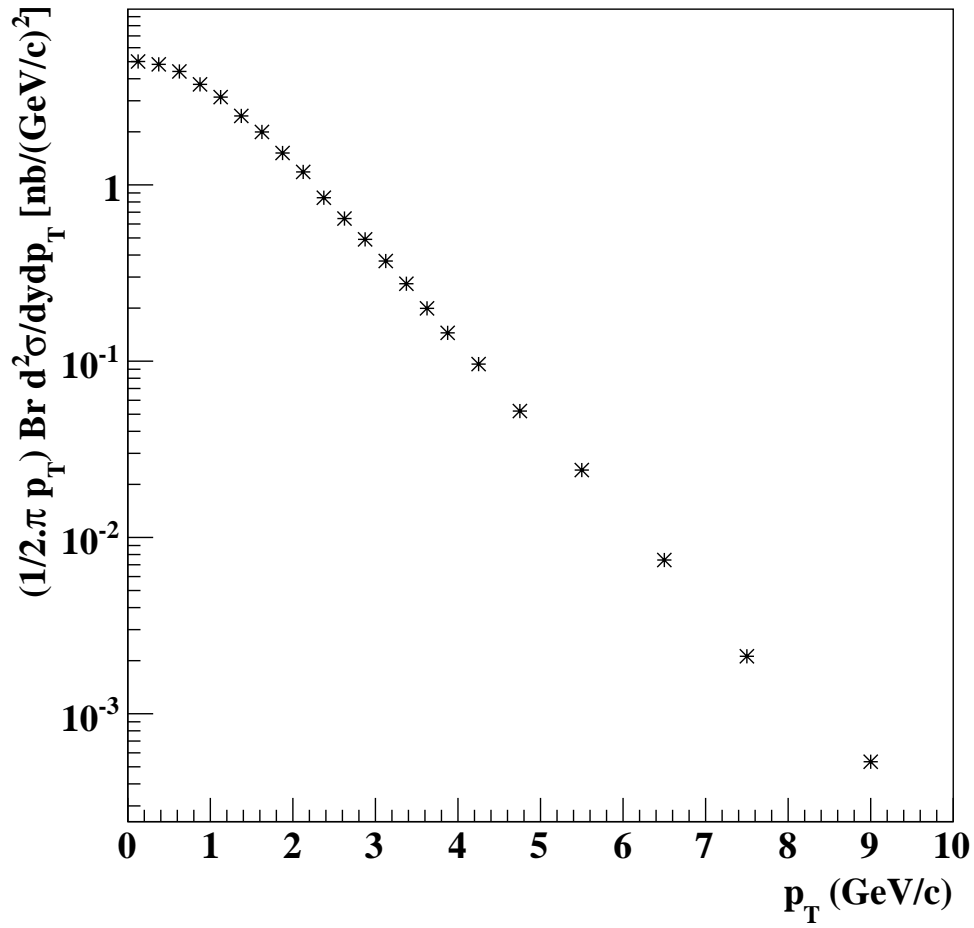


Figure 47: J/ψ differential cross section as a function of p_T averaged over both arms.

6 Systematic Uncertainties

In summary, the following are the dominant systematic uncertainties associated with this measurement:

- **Signal extraction**
A 3.9% systematic uncertainty is assigned to account for the yield variations between using different background fits. This systematic uncertainty is a point-to-point correlated uncertainty. (Type-B).
- **Acceptance/efficiency**
A 12.1% uncertainty for the north arm and 10.3% uncertainty for the south arm are allocated for the $A\varepsilon_{rec}$ and is described in detail in Section 4. This is considered as a Type-B point-to-point correlated uncertainties.
- **MuID and MuTr efficiencies**
Based on previous Muon Arm analyses, a $\pm 4\%$ uncertainty from MuID tube efficiency and an 8.2% (2.8%) for the north (south) arm from MuTr overall efficiency were assigned. These errors are point-to-point correlated (Type-B).
- **$\psi(2S)$ contribution**
A $\sim 3\%$ uncertainty is assigned due to ignoring $\psi(2S)$ contribution.
- **BBC efficiency**
An uncertainty of $\pm 10\%$ was assigned for the overall BBC normalization [15]. This systematic is a global (Type-C) uncertainty that allows the data points to move together by a common multiplicative factor.

From this list, the type-B systematic uncertainties add up to $\sim 16.0\%$ in the north arm and $\sim 12.4\%$ in the south arm. All systematic uncertainties are listed in Table 8.

Table 8: Systematic uncertainties associated with the differential cross section.

Type	Origin	Value
B	Signal extraction	3.9%
B	$A\varepsilon_{rec}$	12.1% (10.3%)
B	MuID hit efficiency	4%
B	MuTr hit efficiency	8.2% (2.8%)
B	$\psi(2S)$ contribution	3%
B	Total	16.0% (12.4%)
C	MB trigger efficiency	10%

7 Results and Comparisons

7.1 Differential cross sections

Figure 48 shows J/ψ differential cross section with the associated systematic uncertainties as a function of p_T in the left panel and as a function of rapidity in the right panel.

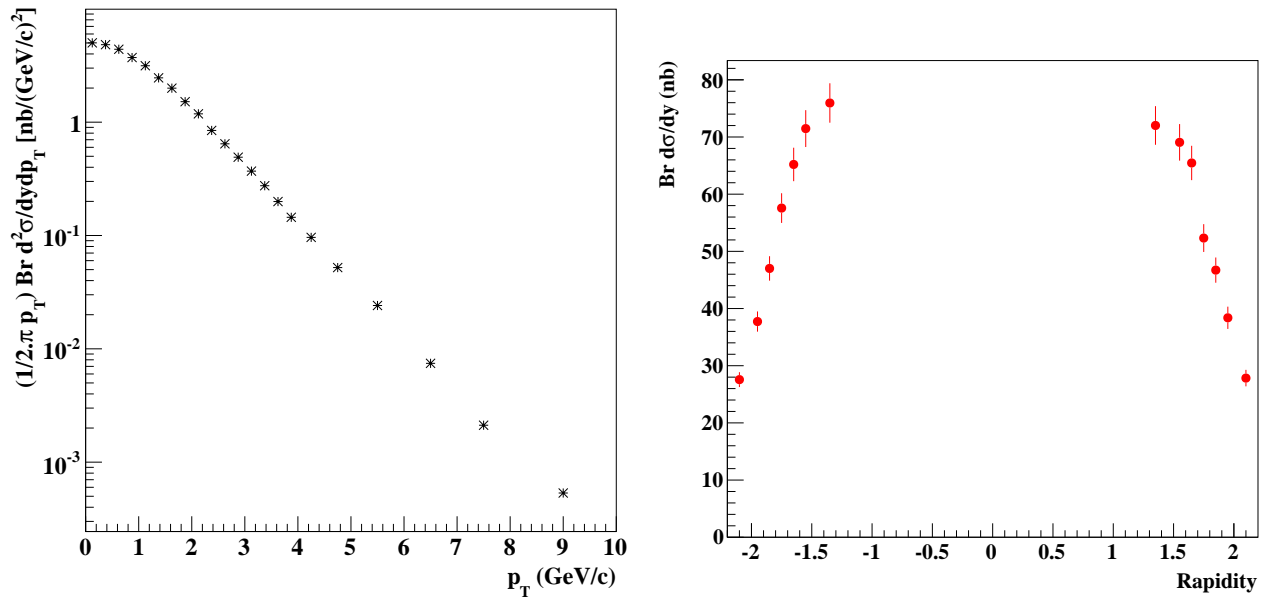


Figure 48: J/ψ differential cross section as a function of p_T (left) and as a function of rapidity (right).

Figure 49 shows the differential cross section from this measurement compared with previous PHENIX J/ψ differential cross section measurement at $\sqrt{s}=200$ GeV [1], and STAR's midrapidity e^-e^+ and $\mu^-\mu^+$ measurements at $\sqrt{s}=500$ GeV [19].

To extract the integrated cross section, $d\sigma/dy$, of J/ψ production at $1.2 < |y| < 2.2$, the p_T dependent differential cross section, $d^2\sigma/dydp_T$, is fitted by the Levy-Tsallis function [18], as shown in Fig. 50. The fit produced, $Br(J/\psi \rightarrow \mu\mu) \times d\sigma/dy(1.2 < |y| < 2.2) = 54.6 \pm 0.5(\text{stat})$ nb. This is consistent with extracting it directly from the p_T -spectra, $Br(J/\psi \rightarrow \mu\mu) \times d\sigma/dy(1.2 < |y| < 2.2) = 54.3 \pm 0.5(\text{stat})$ nb.

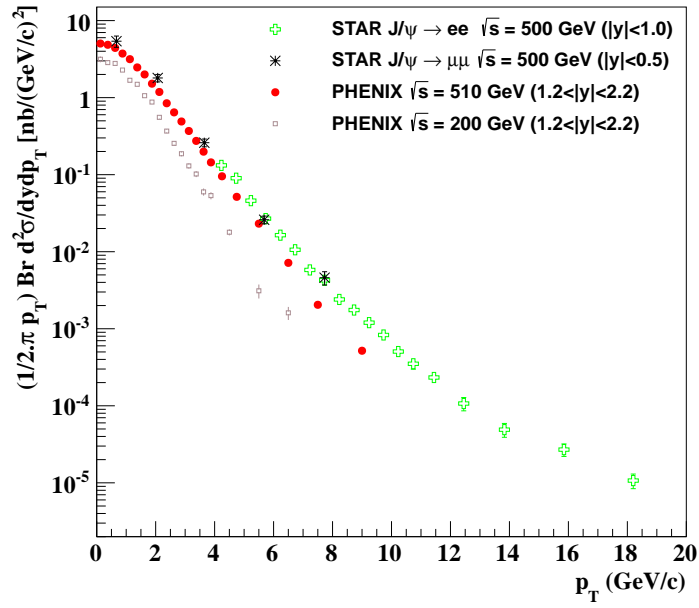
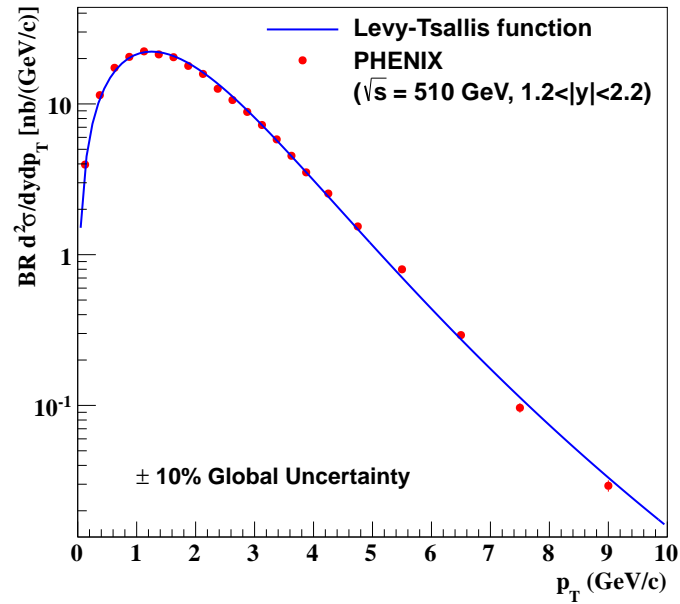
In addition, the data are compared to next-to-leading order calculations in nonrelativistic QCD [20,21] and the results are shown in Figure 51.

Table 9: The weighted average of J/ψ differential cross section as a function of p_T .

p_T (GeV/c)	$\frac{Br}{2\pi p_T} \frac{d^2\sigma}{dy dp_T} \pm \text{stat} \pm \text{sys}$ (nb/[GeV/c ²])
0.00	0.25
0.25	0.50
0.50	0.75
0.75	1.00
1.00	1.25
1.25	1.50
1.50	1.75
1.75	2.00
2.00	2.25
2.25	2.50
2.50	2.75
2.75	3.00
3.00	3.25
3.25	3.50
3.50	3.75
3.75	4.00
4.00	4.50
4.50	5.00
5.00	6.00
6.00	7.00
7.00	8.00
8.00	10.00

Table 10: J/ψ differential cross section as a function of rapidity.

Rapidity	$d\sigma/dy \pm \text{stat} \pm \text{sys}$ (nb)
-2.20	-2.00
-2.00	-1.90
-1.90	-1.80
-1.80	-1.70
-1.70	-1.60
-1.60	-1.50
-1.50	-1.20
-1.20	1.20
1.20	1.50
1.50	1.60
1.60	1.70
1.70	1.80
1.80	1.90
1.90	2.00
2.00	2.20

Figure 49: J/ψ differential cross section as a function of p_T .Figure 50: J/ψ differential cross section as a function of p_T (solid black points) integrated by the Levy-Tsallis function [18] (green line).

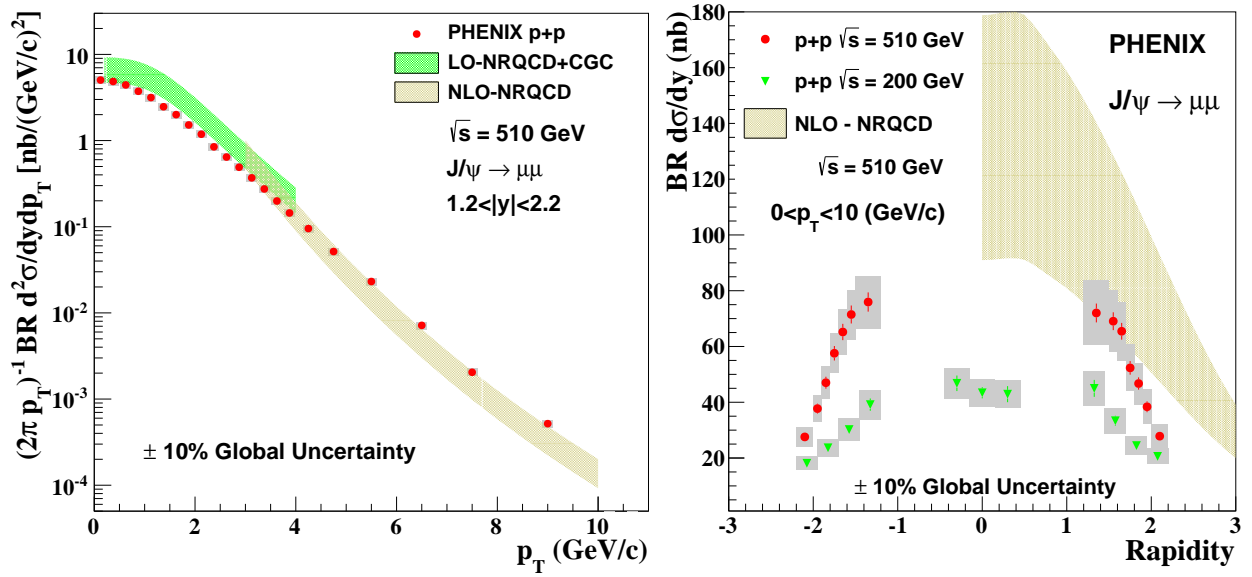


Figure 51: J/ψ differential cross section compared with NLO_NRQCD calculations as a function of p_T (left panel) and as a function of rapidity (right panel).

7.2 $\langle p_T \rangle$ and $\langle p_T^2 \rangle$

To better quantify the hardening of the J/ψ p_T spectra with increasing \sqrt{s} , a computation of the corresponding mean transverse momentum $\langle p_T \rangle$ and mean transverse momentum square $\langle p_T^2 \rangle$ is performed. This is achieved by fitting the J/ψ p_T -differential cross sections with the following function [1, 2]:

$$f(p_T) = A \frac{p_T}{(1 + (\frac{p_T}{B})^2)^n} \quad (12)$$

where A , B and n are free parameters. Figures 52 and 53 show $\langle p_T \rangle$ and $\langle p_T^2 \rangle$, respectively, which for this measurement are the first and second moments of Equation 12 in a given p_T range.

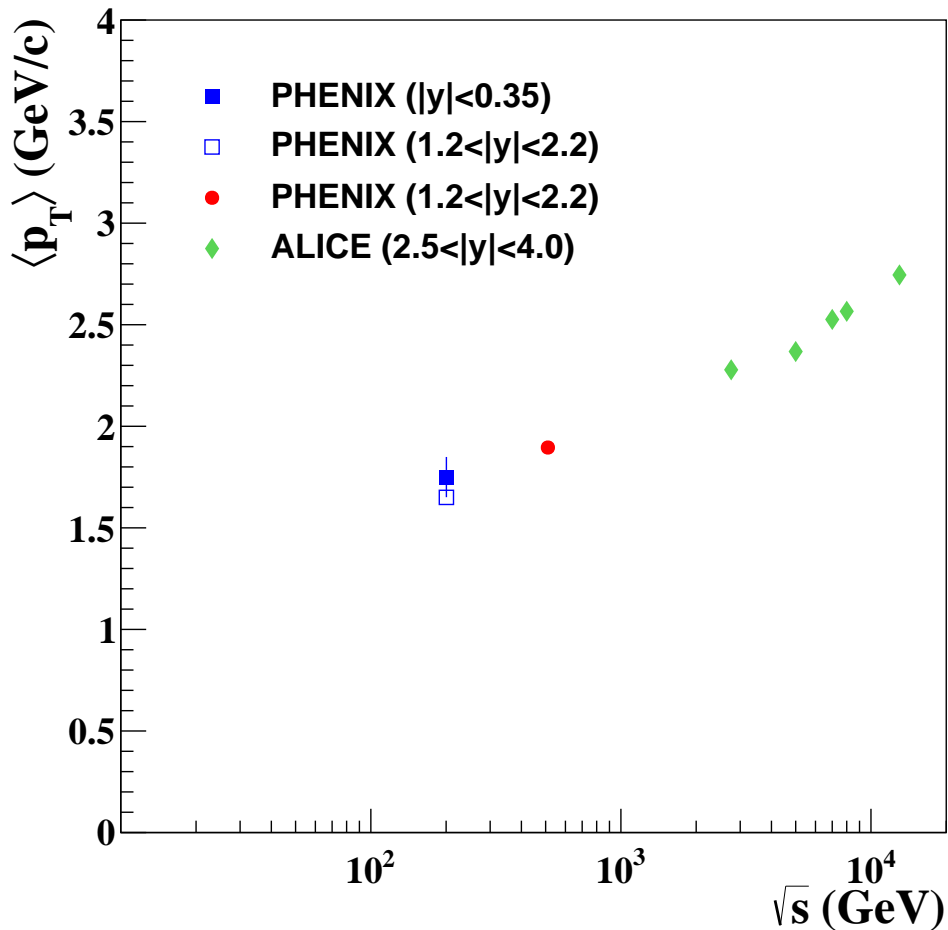


Figure 52: $\langle p_T \rangle$ as a function of \sqrt{s} for J/ψ meson. The figure includes results from this analysis at 510 GeV (solid red points), PHENIX results at 200 GeV [1] at midrapidity (solid blue square) and forward rapidity (empty blue square) and ALICE's data at different energies [2] (solid green diamonds).

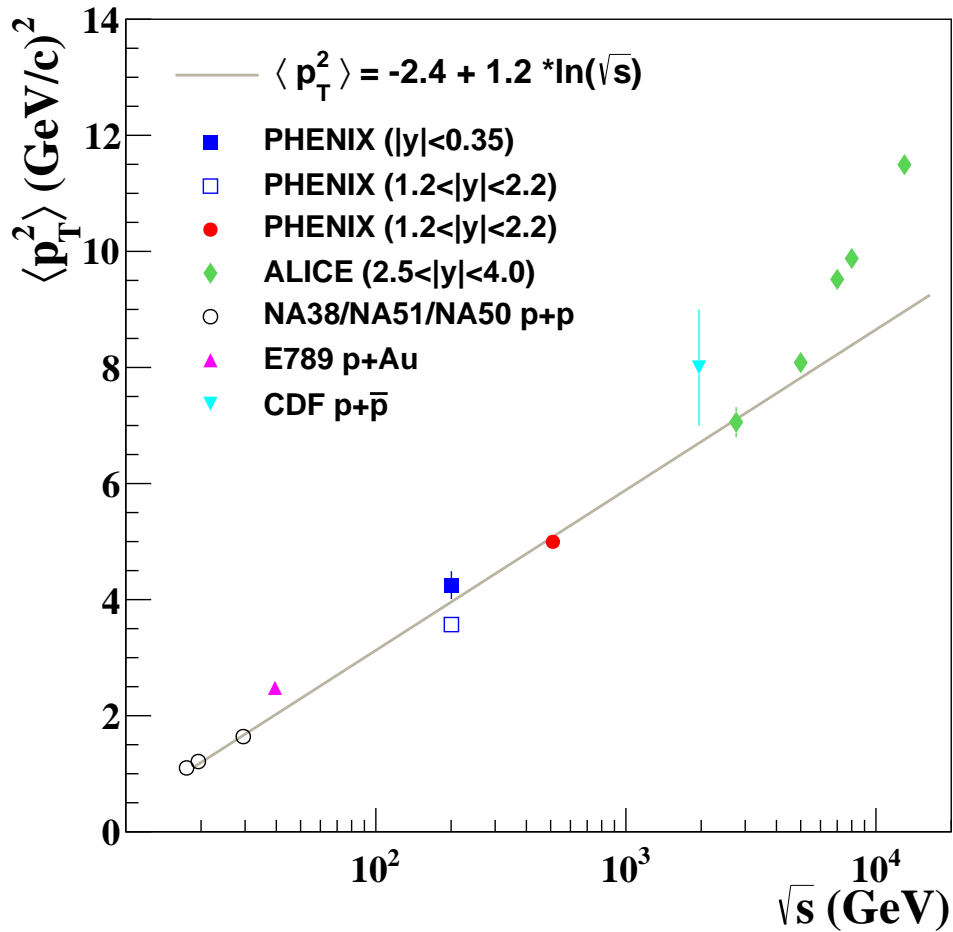


Figure 53: $\langle p_T^2 \rangle$ as a function of \sqrt{s} for J/ψ meson. The figure includes results from this analysis at 510 GeV (solid red points), PHENIX results at 200 GeV [1] at midrapidity (solid blue square) and forward rapidity (empty blue square) and ALICE's data at different energies [2] (solid green diamonds).

7.3 $d\sigma/dy$ vs \sqrt{s}

The differential cross section, $d\sigma/dy$, at $\sqrt{s} = 510$ GeV was compared to PHENIX 200 GeV and those of ALICE's from 2.76 to 13 TeV. ALICE's data were taken at more forward rapidity, $2.5 < y < 4.0$, and to compare them to PHENIX's data at $1.2 < y < 2.2$, the $d\sigma/dy$ ($1.2 < y < 2.2$) was extracted by fitting ALICE's data (both forward, backward and midrapidity) at each energy with $d\sigma/dy$ extracted from Pythia. Fig. 54 shows the J/ψ p_T and y -integrated inclusive cross sections as a function of \sqrt{s} . A steady increase of $d\sigma/dy$ is observed as a function of increasing \sqrt{s} .

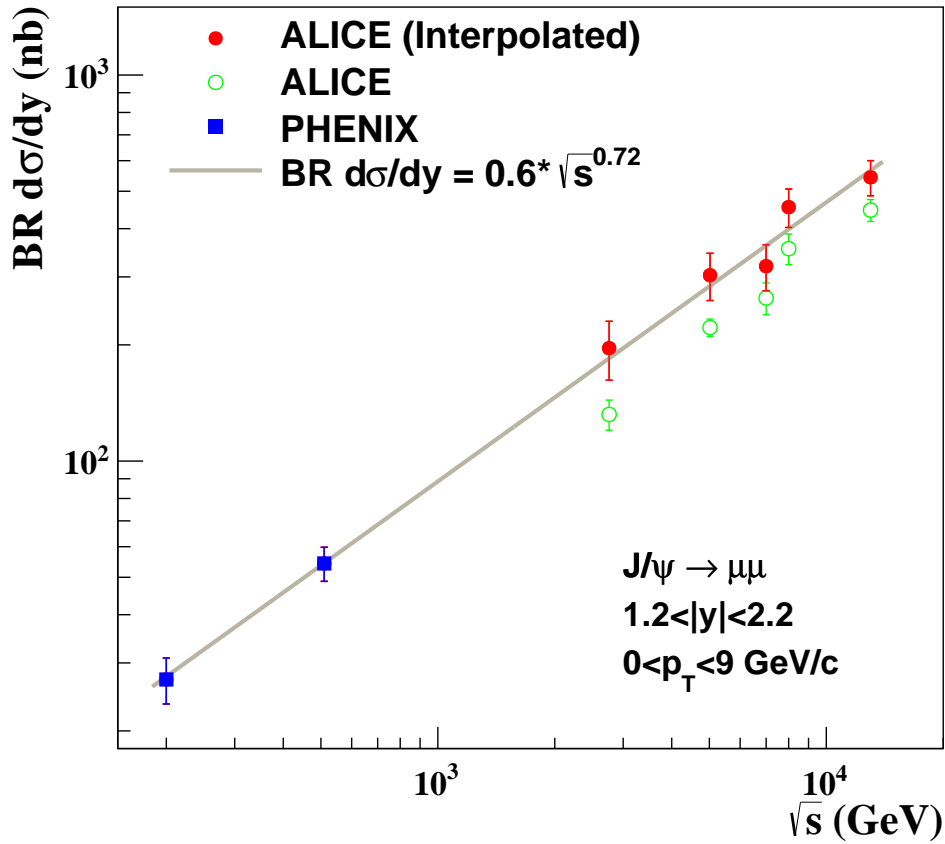


Figure 54: $d\sigma/dy$ as a function of \sqrt{s} . Vertical lines correspond to the quadratic sum of the statistical and uncorrelated systematic uncertainties.

References

- [1] A. Adare et al. J/ψ Production versus Transverse Momentum and Rapidity in $p+p$ Collisions at $\sqrt{s}=200$ GeV. *Phys. Rev. Lett.*, 98:232002, 2007. 1, 7.1, 7.2, 52, 53
- [2] S. Acharya et al. Energy dependence of forward-rapidity J/ψ and $\psi(2S)$ production in pp collisions at the LHC. 1, 7.2, 52, 53
- [3] Harald Fritzsche. Producing heavy quark flavors in hadronic collisions— A test of quantum chromodynamics. *Phys. Lett. B*, 67(2):217 – 221, 1977. 1
- [4] J.F. Amundson, O.J.P. Éboli, E.M. Gregores, and F. Halzen. Quantitative tests of color evaporation: charmonium production. *Phys. Lett. B*, 390(1):323 – 328, 1997. 1
- [5] R. Baier and R. R uckl. Hadronic production of J/ψ and v : Transverse momentum distributions. *Phys. Lett. B*, 102(5):364 – 370, 1981. 1
- [6] Geoffrey T. Bodwin, Eric Braaten, and G. Peter Lepage. Rigorous QCD analysis of inclusive annihilation and production of heavy quarkonium. *Phys. Rev. D*, 51:1125–1171, 1995. 1
- [7] C. Aidala et al. Measurements of $B \rightarrow J/\psi$ at forward rapidity in $p + p$ collisions at $\sqrt{s} = 510$ GeV. *Phys. Rev. D*, 95:092002, 2017. 1
- [8] C. Aidala et al. Angular decay coefficients of J/ψ mesons at forward rapidity from $p+p$ collisions at $\sqrt{s} = 510$ GeV. *arXiv:1612.06807*. 1
- [9] M. Beaumier, F. Giordano, R. Hollis, D. Jumper, A. Meles, and R. Seidl. Run 13 $W \rightarrow \mu$ Analysis, Single Spin Asymmetry and cross section. *PHENIX Analysis note: AN1195*. 2.1, 5
- [10] S. Park and R. Seidl. Update of the Run12 and 13 W to μ analysis note and finalization of results. *PHENIX Analysis note: AN1327*. 2.1, 4.1
- [11] R. Tieulent, X. He, M. Jezghani, and M. Sarsour. ϕ meson production cross section in pp collisions at $\sqrt{s} = 510$ GeV and its energy dependence. *PHENIX Analysis note: AN1232*. 2.2, 3.2.1
- [12] A. Sen, X. He, L. Patel, and J. Ying. J/ψ Dimuon Measurement from Run10 Au+Au Collisions at 62 and 39 GeV. *PHENIX Analysis note: AN975*. 3.2.2
- [13] M. Leitch et al. $J/\psi \rightarrow \mu\mu$ Invariant yields using Run-6 $p+p$ and Run-8 $d+Au$ at $\sqrt{s_{NN}} = 200$ GeV. PHENIX Analysis note: AN794. 4
- [14] M. Sarsour, X. He, M. Jezghani, and R. Tieulent. Low Mass Vector Meson Measurement in $d+Au$ Collisions at 200 GeV in the PHENIX Muon Arms. *PHENIX Analysis note: AN1166*. 4
- [15] A. Datta and D. Kawall. σ_{BBC} using Vernier scans for 500 GeV pp Data in Run 9. *PHENIX Analysis note: AN888*. 5, 6
- [16] K. Nakamura et al. Review of Particle Physics. *J. Phys. G*, 37:075021, 2010. 5
- [17] G.D. Lafferty and T.R. Wyatt. Where to stick your data points: The treatment of measurements within wide bins. *Nucl. Instrum. Methods Phys. Res., Sect. A*, 355:541 – 547, 1995. 5
- [18] A. Adare et al. Measurement of neutral mesons in $p + p$ collisions at $\sqrt{s} = 200$ GeV and scaling properties of hadron production. *Phys. Rev. D*, 83:052004, 2011. 5, 46, 5, 7.1, 50
- [19] J. Adam et al. Measurements of the transverse-momentum-dependent cross sections of j/ψ production at mid-rapidity in proton + proton collisions at $\sqrt{s} = 510$ and 500 geV with the star detector. *Phys. Rev. D*, 100:052009, 2019. 7.1

-
- [20] Yan-Qing Ma, Kai Wang, and Kuang-Ta Chao. $J/\psi(\psi')$ Production at the Tevatron and LHC at $\mathcal{O}(\alpha_s^4 v^4)$ in Nonrelativistic QCD. *Phys. Rev. Lett.*, 106:042002, 2011. 7.1
- [21] Xuan Li. Private communication. 7.1

Appendix

A Run Lists

601 runs survived the QA and TAXI run and are listed below:

386775 386776 386777 386825 386826 386828 386829 386830 386833 386838 386839 386841 386843 386844 386881
 386882 386883 386884 386941 386942 386943 386946 386947 386948 386951 386952 387070 387077 387078 387139
 387227 387247 387290 387292 387414 387430 387431 387433 387436 387539 387541 387543 387550 387560 387566
 387571 387649 387651 387658 387659 387660 387661 387668 387669 387670 387672 387673 387674 387676 387710
 387719 387724 387725 387784 387785 387787 387790 387792 387793 387802 387803 387808 387809 387963 387967
 387968 388019 388021 388022 388023 388038 388039 388042 388047 388050 388051 388052 388261 388263 388265
 388266 388404 388405 388495 388536 388539 388540 388541 388547 388548 388632 388633 388634 388638 388640
 388692 388693 388694 388697 388698 388699 388700 388720 388721 388724 388726 388743 388837 388838 388840
 388859 388860 388862 388863 388865 388866 388978 388980 388981 388984 388985 388986 389119 389120 389121
 389123 389124 389126 389320 389322 389323 389324 389326 389327 389334 389335 389336 389338 389339 389424
 389434 389436 389444 389445 389446 389471 389560 389570 389571 389573 389575 389577 389578 389579 389586
 389587 389589 389590 389702 389703 389752 389756 389758 389759 389761 389762 389766 389767 389768 390510
 390518 390519 390537 390538 390540 390541 390542 390615 390667 390669 390670 390674 390942 390943 390944
 390954 390958 390959 390963 390964 390965 391036 391041 391047 391051 391169 391170 391174 391177 391291
 391371 391374 391377 391442 391445 391446 391465 391466 391470 391471 391566 391569 391579 391583 391588
 391722 391813 391815 391860 391861 391873 391875 391876 391966 391968 391969 391982 392015 392027 392028
 392226 392267 392292 392293 392297 392299 392359 392415 392418 392420 392422 392428 392429 392540 392541
 392542 392545 392548 392811 392814 392818 392819 392821 392838 392840 392842 392846 392848 392922 392926
 392928 392934 392942 392947 393051 393054 393056 393061 393062 393066 393067 393164 393167 393175 393176
 393177 393178 393180 393341 393342 393343 393345 393349 393351 393458 393461 393462 393464 393469 393471
 393478 393481 393483 393484 393485 393486 393487 393529 393530 393531 393534 393574 393575 393576 393577
 393581 393627 393677 393795 393798 393805 393809 393810 393883 393885 393888 393890 393891 393898 393901
 393905 394002 394003 394004 394005 394048 394049 394050 394054 394055 394057 394060 394061 394062 394065
 394066 394067 394068 394069 394072 394272 394388 394389 394391 394398 394400 394402 394417 394420 394421
 394423 394526 394538 394539 394676 394679 394682 394683 394684 394698 394700 394701 394702 394704 394739
 394742 394744 394745 394750 394962 394980 395099 395228 395230 395231 395233 395238 395239 395244 395389
 395396 395397 395402 395405 395407 395408 395411 395412 395413 395420 395432 395526 395527 395544 395545
 395550 395551 395553 395587 395588 395590 395591 395592 395594 395595 395599 395639 395640 395641 395643
 395645 395646 395731 395732 395769 395771 395775 395777 395808 395809 395811 395813 395816 395817 395882
 395884 395899 395901 395907 395908 395939 395940 396048 396049 396054 396056 396058 396065 396066 396073
 396074 396075 396268 396274 396277 396279 396280 396363 396366 396412 396415 396418 396433 396434 396437
 396438 396440 396544 396545 396546 396549 396552 396560 396612 396614 396616 396617 396618 396619 396627
 396628 396629 396630 396631 396633 396634 396635 396636 396677 396678 396681 396682 396683 396684 396760
 396761 396764 396765 396766 396767 396768 396785 396790 396799 396802 396803 396887 396889 396891 396910
 396914 396919 396921 396993 396994 397000 397049 397066 397069 397070 397176 397178 397181 397184 397201
 397208 397290 397291 397294 397297 397313 397315 397317 397318 397319 397322 397401 397402 397431 397432
 397433 397434 397437 397438 397511 397513 397517 397519 397524 397525 397526 397527 397531 397532 397534
 397535 397581 397587 397588 397589 397692 397700 397705 397708 397710 397711 397712 397715 397735 397738
 397866 397933 397934 397938 397989 397990 398005 398007 398009 398011 398013 398014 398018 398019 398020
 398026 398119 398122 398124 398125 398130 398133 398137 398138 398142 398144 398145 398146 398147 398148
 398149

B PYTHIA Cards

Table B1: PYTHIA control data card for J/ψ .

roots	510			
proj	p			
targ	p			
frame	cms			
mset	0			turn on all prod. mechanisms manually
msub	86	1		$g+g \rightarrow J/\psi$
pmas	4	1	1.25	
mdme	858	1	0	$J/\psi \rightarrow ee$ turned off
mdme	859	1	1	$J/\psi \rightarrow \mu\mu$ turned on
mdme	860	1	0	$J/\psi \rightarrow$ random turned off
mstp	51	10041		CTEQ6LL
mstp	52	2		use LHAPDF
parp	91	2.1		set intrinsic k_T value

C Scaled down runs

Table C1: Runs that have muon 2D trigger scaled down.

Run No.	Scale Down
388978	1
391169	1
391291	1
391442	1
391566	1
391722	1
391813	5
391815	1
391982	1
392015	1
393478	2
394048	1
394417	1
394526	1
394682	5
394683	1
394739	1
394962	1
395587	1
395639	1
395731	1
395882	1
396056	1
396760	1
396993	1
397290	1
397989	1
398005	1
398130	1